Extended data for

A Library of High-Entropy-Alloy Nanocrystals with Controlled Surface Atomic Arrangements for Catalysis

Yueh-Chun Hsiao,[1,2] Cheng-Yu Wu,[1] Wen-Yang Huang,[3] Ho Viet Thang,[4,5] Chong-Chi Chi,[6] Wen-Jing Zeng,[3] Jia-Qi Gao,[1] Chih-Yi Lin,[1] Jui-Tai Lin,[1] Chih-Heng Lee,[4] Islam M. A. Mekhemer,[1] Ming-Yen Lu,[6,7] Ying-Rui Lu,[8] Ho-Hsiu Chou,[1] Shan Zhou,[9] Hsin-Yi Tiffany Chen,[4,7,10,]* Alexander J. Cowan,[2,]* Sung-Fu Hung,[3,]* Jien-Wei Yeh,[7,11,]* and Tung-Han Yang[1,]*

[1]Department of Chemical Engineering, National Tsing Hua University, Hsinchu 30013, Taiwan.

[2]Stephenson Institute for Renewable Energy and Department of Chemistry, University of Liverpool, Liverpool L69 7ZF, United Kingdom.

[3]Department of Applied Chemistry, National Yang Ming Chiao Tung University, Hsinchu 30013, Taiwan.

[4]Department of Engineering and System Science, National Tsing Hua University, Hsinchu 30013, Taiwan.

[5]The University of Da Nang, University of Science and Technology, 54 Nguyen Luong Bang, Danang 550000, Vietnam.

[6]Instrumentation Center, National Tsing Hua University, Hsinchu 30013, Taiwan.

[7]Department of Materials Science and Engineering, National Tsing Hua University, Hsinchu 30013, Taiwan.

[8]National Synchrotron Radiation Research Center, Hsinchu 300, Taiwan.

[9]Department of Nanoscience and Biomedical Engineering, South Dakota School of Mines and Technology, Rapid City, South Dakota 57701, United States.

[10]College of Semiconductor Research, National Tsing Hua University, Hsinchu 30013, Taiwan.

[11]High Entropy Materials Center, National Tsing Hua University, Hsinchu 30013, Taiwan.

*Corresponding author. Email: tunghanyang@mx.nthu.edu.tw; jwyeh@mx.nthu.edu.tw; sungfuhung@nycu.edu.tw; acowan@liverpool.ac.uk; hsinyi.tiffany.chen@gapp.nthu.edu.tw

The extended data include: Figures S1 to S30, Tables S1 to S9, and References

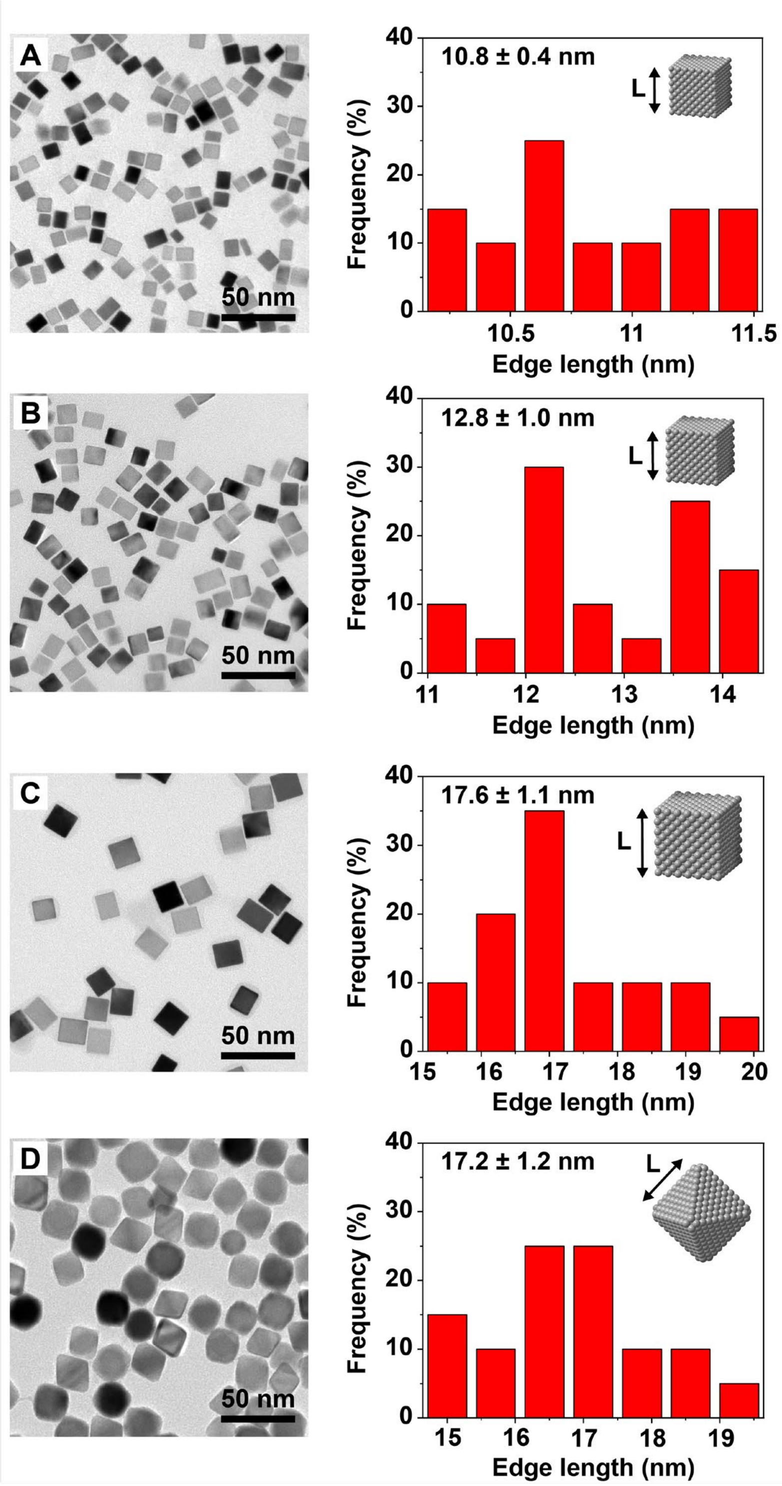

Figure S1. TEM images of Pd seeds and their edge length distributions. (A) 10.8-nm Pd cubic seeds. (B) 12.8-nm Pd cubic seeds. (C) 17.6-nm Pd cubic seeds. (D) 17.2-nm Pd octahedral seeds. Schematic illustrations in the figures showing particle size (L) was defined for a cube and octahedron.

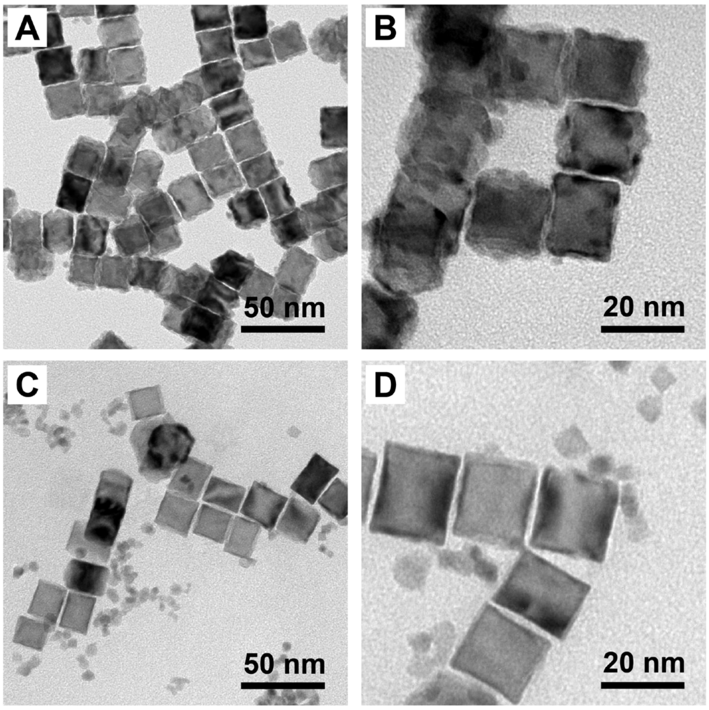

Figure S2. (A) Low and (B) high magnification TEM images of Pd@$Pd_{0.2}Pt_{0.2}Ir_{0.2}Ru_{0.2}Rh_{0.2\text{-}4L}$ core-shell nanocubes from the synthesis conducted at a lower reaction temperature of 180 ºC, while keeping all other experimental parameters the same (concentration of each metal precursor equals to 0.042 μmol mL^{-1}). It can be seen that the formation of islands randomly distributed on the Pd nanocubes, implying a higher reaction temperature of 195 ºC is required to facilitate surface diffusion to obtain the conformal coating of HEA layers on the Pd cubic seeds. (C) Low and (D) high magnification TEM images of Pd@$Pd_{0.2}Pt_{0.2}Ir_{0.2}Ru_{0.2}Rh_{0.2\text{-}4L}$ core-shell nanocubes from the synthesis conducted at a faster injection rate of 3.2 mL h^{-1}, while keeping all other experimental parameters the same. There were many tiny, self-nucleated nanoparticles, together with the core-shell cubic nanocrystals.

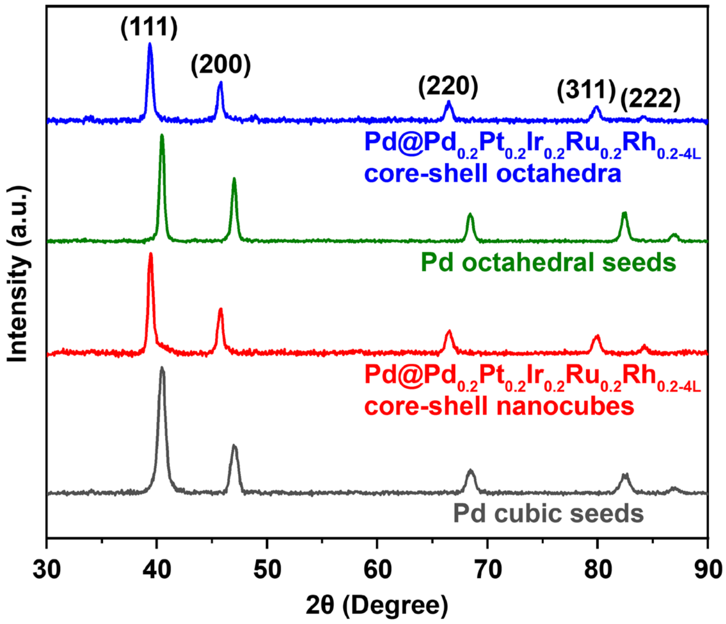

Figure S3. XRD patterns of Pd cubic and octahedral seeds, as well as the $Pd@Pd_{0.2}Pt_{0.2}Ir_{0.2}Ru_{0.2}Rh_{0.2\text{-}4L}$ core-shell nanocubes and octahedra. The patterns revealed that the Pd seeds and Pd@HEA nanocrystals all have a face-centered cubic (fcc) structure. The peak positions shifted after the deposition of HEA shells on the Pd seeds, together with a slight decrease in peak intensity.

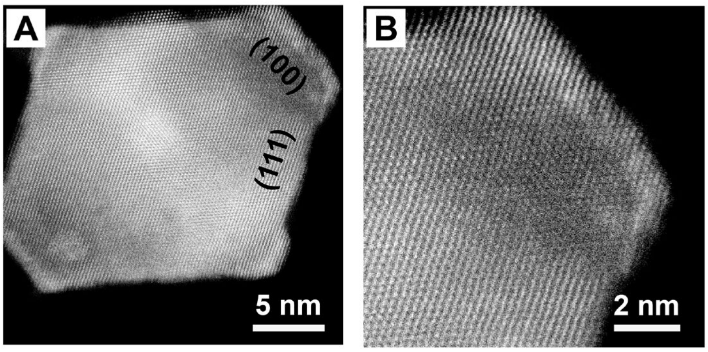

Figure S4. (A) Low and (B) high magnification HAADF-STEM images of $Pd@Pd_{0.2}Pt_{0.2}Ir_{0.2}Ru_{0.2}Rh_{0.2\text{-}4L}$ core-shell octahedral nanocrystals sampled at the early stage of $t = 10$ h from the synthesis conducted at 195 °C. It can be seen that more atomic layers of metal atoms were deposited on the {100} facets at the corner sites than the {111} facets at the side faces. This result could be attributed to the different surface free energies of {100} and {111} facets[1].

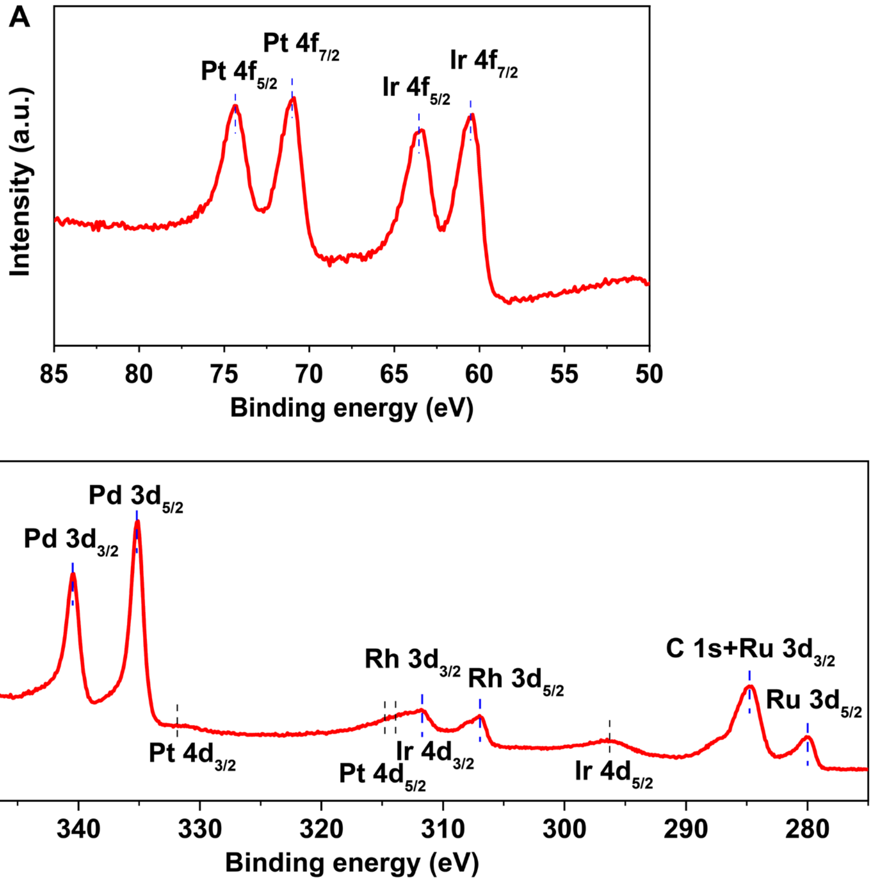

Figure S5. XPS analysis of Pd@Pd$_{0.2}$Pt$_{0.2}$Ir$_{0.2}$Ru$_{0.2}$Rh$_{0.2\text{-}4L}$ core-shell octahedral nanocrystals in the regions of (A) 50-85 eV and (B) 275-360 eV. In the binding energy region of 50-85 eV, the characteristic peaks of Ir 4f and Pt 4f doublets were observed. In the binding energy region of 275-360 eV, the 3d doublets from Ru, Rh, and Pd were resolved as the main peaks along with the weak Pt 4d and Ir 4d signals (black lines). The peak profiles and positions of these five elements in the XPS spectra were in line with their bulk metals, suggesting all elements were in the metallic state[2].

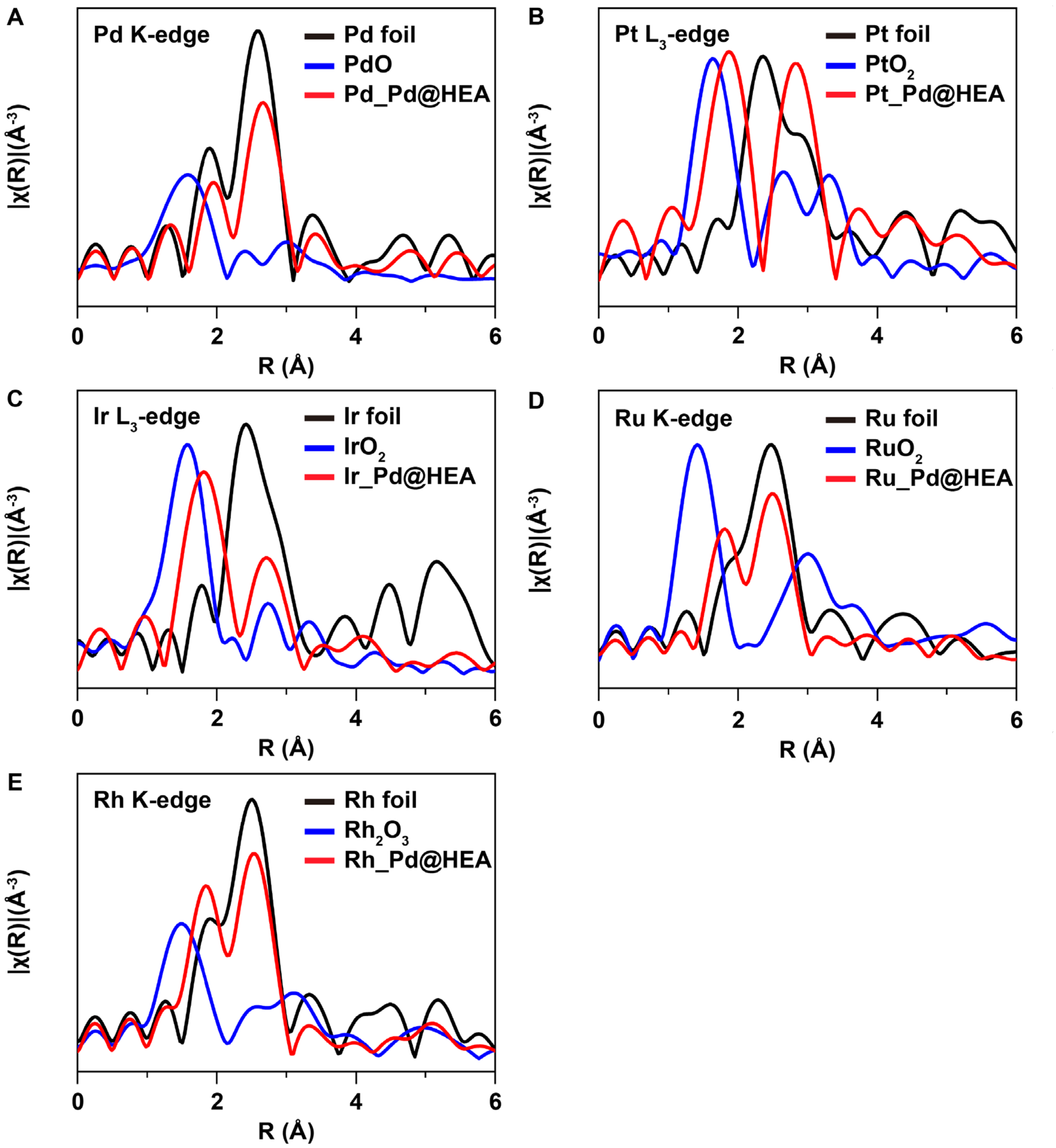

Figure S6. Fourier-transformed extended EXAFS spectra of Pd@$Pd_{0.2}Pt_{0.2}Ir_{0.2}Ru_{0.2}Rh_{0.2}$-4L core-shell nanocubes and the corresponding metallic foil and oxidation state at the (A) Pd K-edge, (B) Pt L_3-edge, (C) Ir L_3-edge, (D) Ru K-edge, and (E) Rh K-edge. In these spectra, there were no significant peaks relating to metal-oxygen interaction (typically, the radial distance is around 1.5 Å), suggesting all elements existed in the metallic state rather than the oxidized form[3,4]. All the spectra for Pd@$Pd_{0.2}Pt_{0.2}Ir_{0.2}Ru_{0.2}Rh_{0.2}$-4L core-shell nanocubes showed typical alloy doublet peaks positioning at Pd (1.96 Å, 2.67 Å), Pt (1.87 Å, 2.82 Å), Ir (1.81 Å, 2.72 Å), Ru (1.81 Å, 2.50 Å), and Rh (1.84 Å, 2.52 Å), respectively.

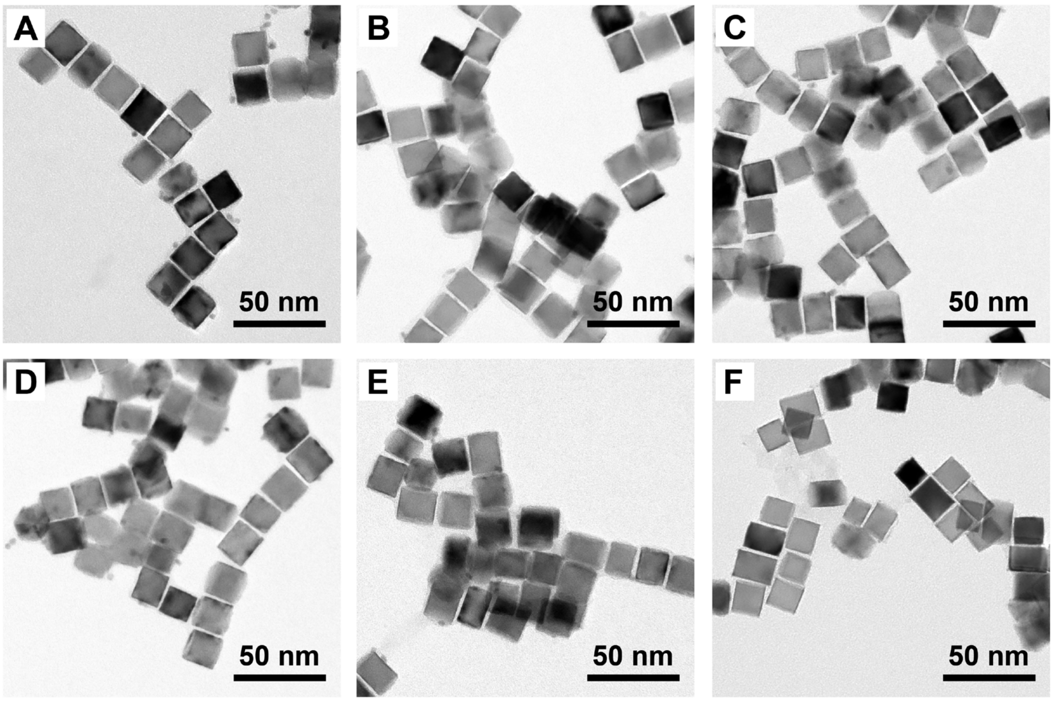

Figure S7. TEM images of six compositional stoichiometries of quinary Pd@PdPtIrRuRh core-shell cubic nanocrystals. These nanocrystals could be obtained by adjusting the ratios of metal precursors added into the synthesis under the standard procedures. (A) Pd@$Pd_{0.225}Pt_{0.1}Ir_{0.225}Ru_{0.225}Rh_{0.225\text{-}4L}$, (B) Pd@$Pd_{0.2}Pt_{0.2}Ir_{0.2}Ru_{0.2}Rh_{0.2\text{-}4L}$, (C) Pd@$Pd_{0.175}Pt_{0.3}Ir_{0.175}Ru_{0.175}Rh_{0.175\text{-}4L}$, (D) Pd@$Pd_{0.15}Pt_{0.4}Ir_{0.15}Ru_{0.15}Rh_{0.15\text{-}4L}$, (E) Pd@$Pd_{0.125}Pt_{0.5}Ir_{0.125}Ru_{0.125}Rh_{0.125\text{-}4L}$, and (F) Pd@$Pd_{0.1}Pt_{0.6}Ir_{0.1}Ru_{0.1}Rh_{0.1\text{-}4L}$ core-shell nanocubes.

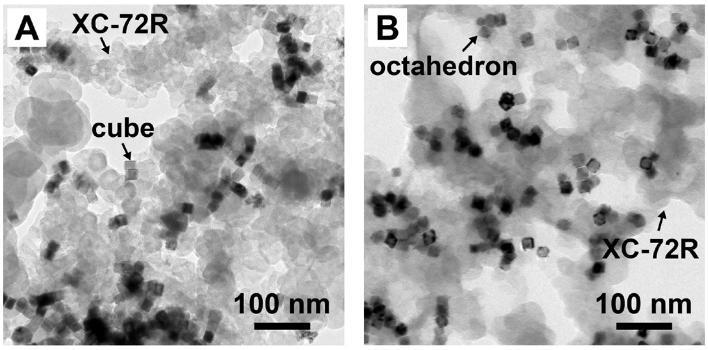

Figure S8. TEM images of Pd@$Pd_{0.2}Pt_{0.2}Ir_{0.2}Ru_{0.2}Rh_{0.2\text{-}4L}$ core-shell (A) nanocubes and (B) octahedra supported on the carbon black (Vulcan XC-72R). These observations suggest the uniform dispersion of Pd@HEA nanocrystals on the supports.

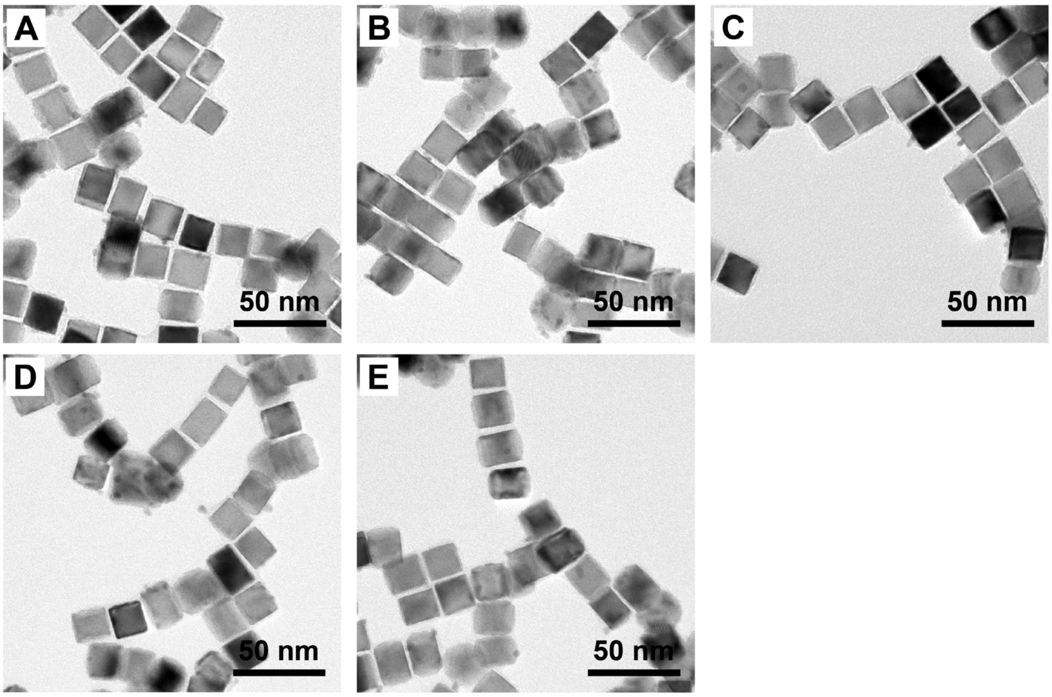

Figure S9. TEM images of (A) Pd@Pd, (B) Pd@Pt, (C) Pd@Ir, (D) Pd@Ru, and (E) Pd@Rh core-shell nanocubes.

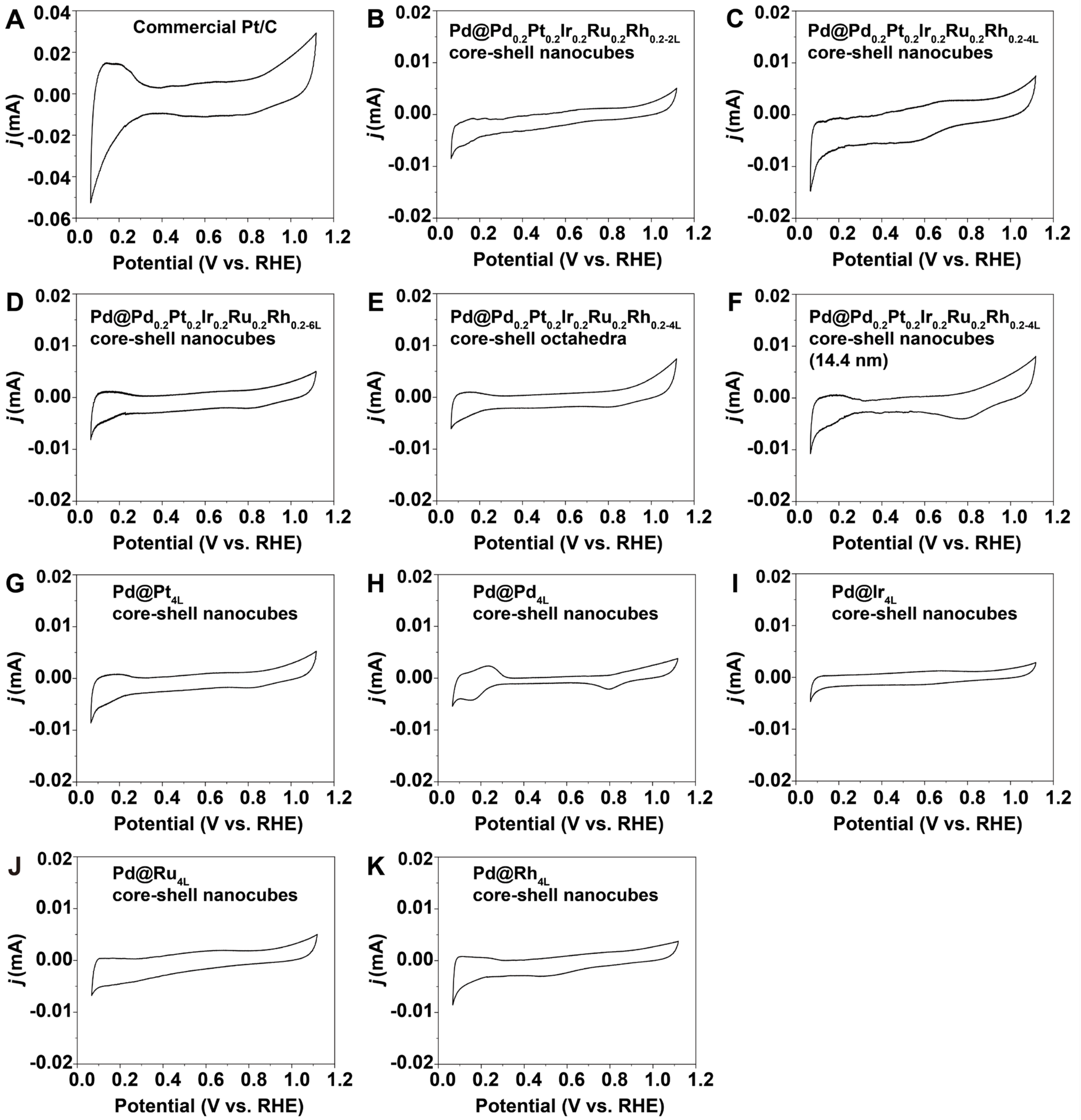

Figure S10. Cyclic voltammetry (CV) curves of Pd@Pd$_{0.2}$Pt$_{0.2}$Ir$_{0.2}$Ru$_{0.2}$Rh$_{0.2\text{-nL}}$ core-shell nanocubes and octahedra, commercial Pt/C, and monometallic samples. The ECSA could be calculated *via* the hydrogen absorption-desorption regions of the corresponding CV curves from 0.05 to 0.40 V.

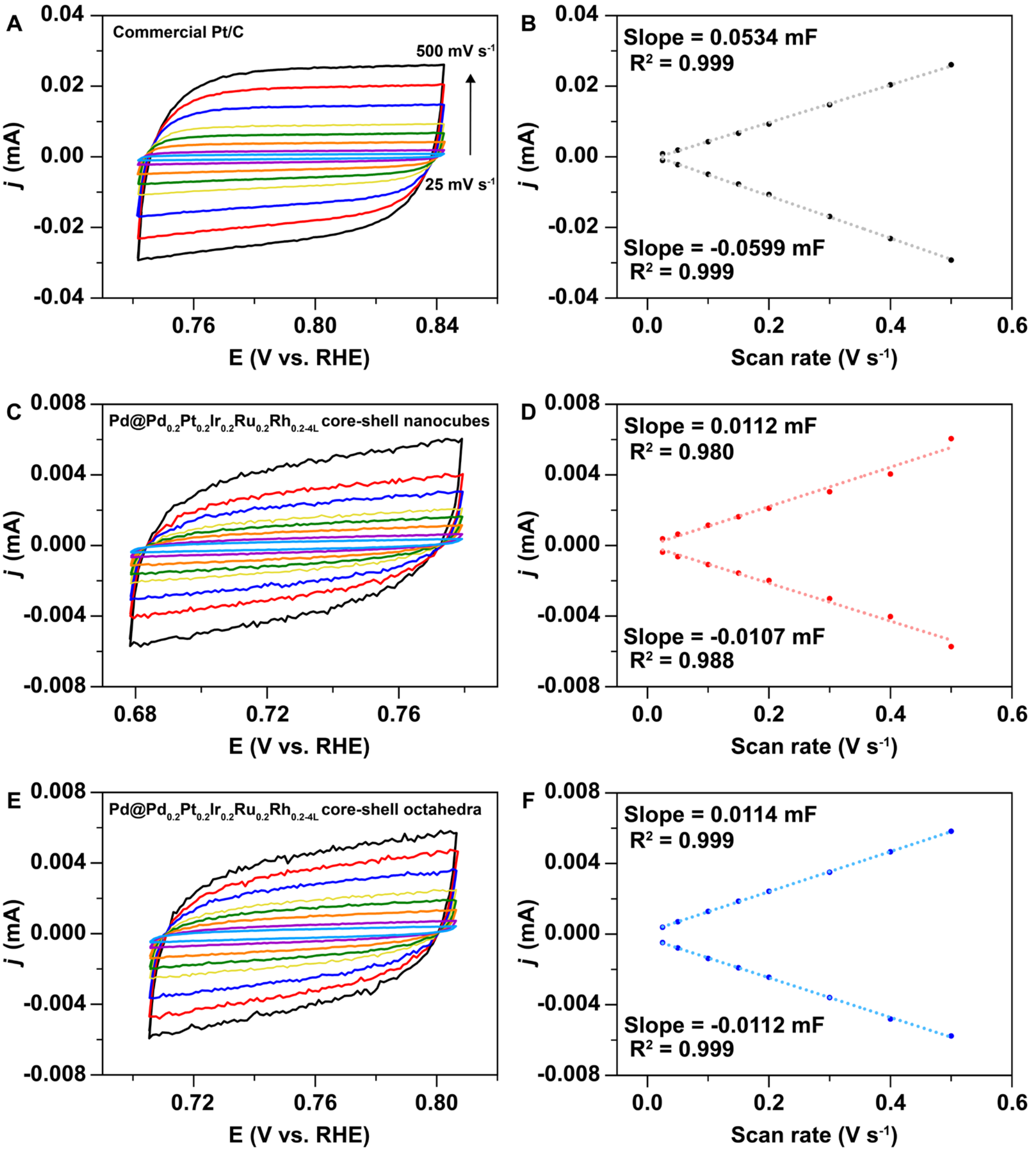

Figure S11. Cyclic voltammograms analysis for determining the double-layer capacitance. CV curves at the scan rate from 25 mV s^{-1} to 500 mV s^{-1} and the anodic and cathodic current distribution as a function of scan rate for commercial Pt/C (A, B), $Pd@Pd_{0.2}Pt_{0.2}Ir_{0.2}Ru_{0.2}Rh_{0.2\text{-}4L}$ core-shell nanocubes (C, D), and $Pd@Pd_{0.2}Pt_{0.2}Ir_{0.2}Ru_{0.2}Rh_{0.2\text{-}4L}$ core-shell octahedra (E, F). The ECSA for the catalysts was linearly proportional to the values of C_{dl} (ECSA = C_{dl}/C_s, C_s is specific capacitance)[5]. In this work, the relationship of C_{dl} between commercial Pt/C (0.0566 mF), $Pd@Pd_{0.2}Pt_{0.2}Ir_{0.2}Ru_{0.2}Rh_{0.2\text{-}4L}$ core-shell nanocubes (0.0109 mF), and $Pd@Pd_{0.2}Pt_{0.2}Ir_{0.2}Ru_{0.2}Rh_{0.2\text{-}4L}$ core-shell octahedra (0.0113 mF) was positively correlated to the ECSA derived from the hydrogen underpotential deposition method, where the ECSA were 29.13 m^2 g^{-1}, 3.78 m^2 g^{-1}, and 4.57 m^2 g^{-1}, respectively.

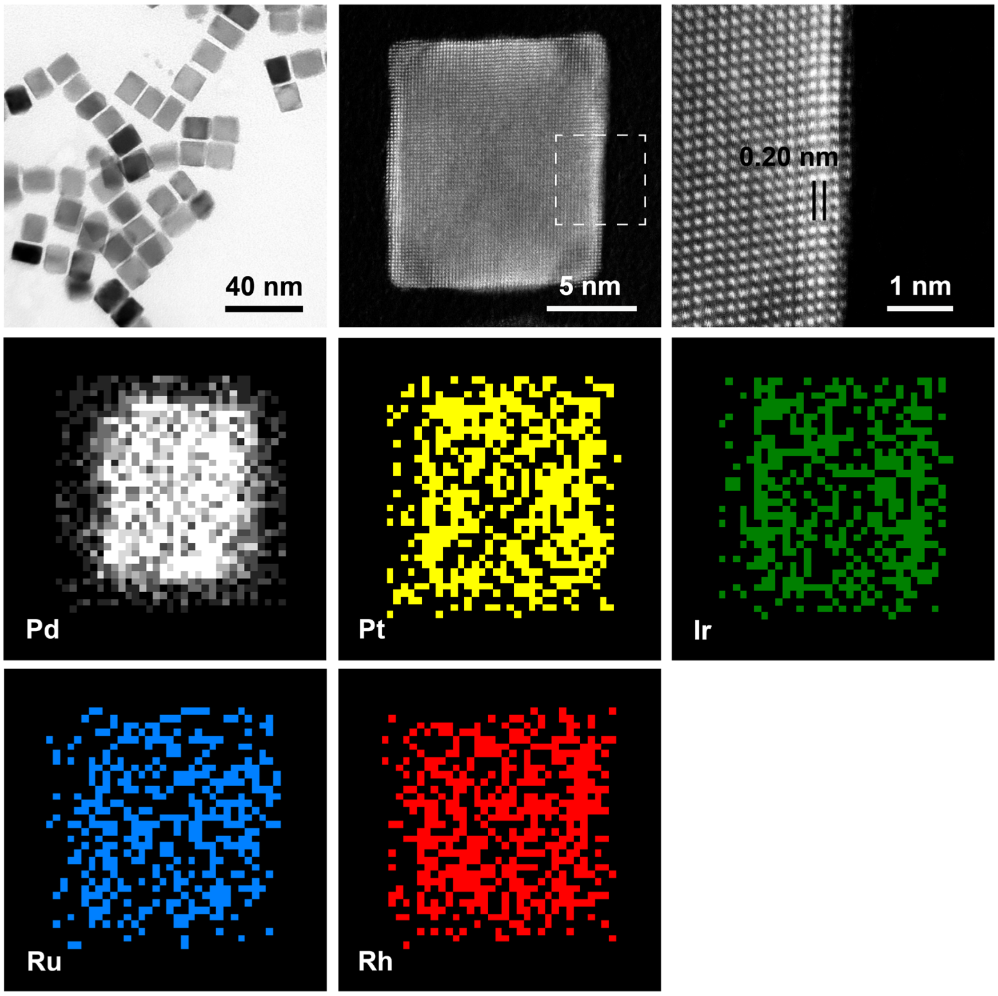

Figure S12. TEM, HAADF-STEM images, and EDS maps of Pd@$Pd_{0.2}Pt_{0.2}Ir_{0.2}Ru_{0.2}Rh_{0.2\text{-}4L}$ core-shell nanocubes (14.4 nm). From the atomic-resolution HAADF-STEM image, the number of Pd@$Pd_{0.2}Pt_{0.2}Ir_{0.2}Ru_{0.2}Rh_{0.2}$ atomic layers with a lattice spacing of around 0.20 nm along the [100] direction was estimated to be 4. Additionally, the EDS maps showed all the deposited elements were uniformly distributed throughout the entire HEA shell.

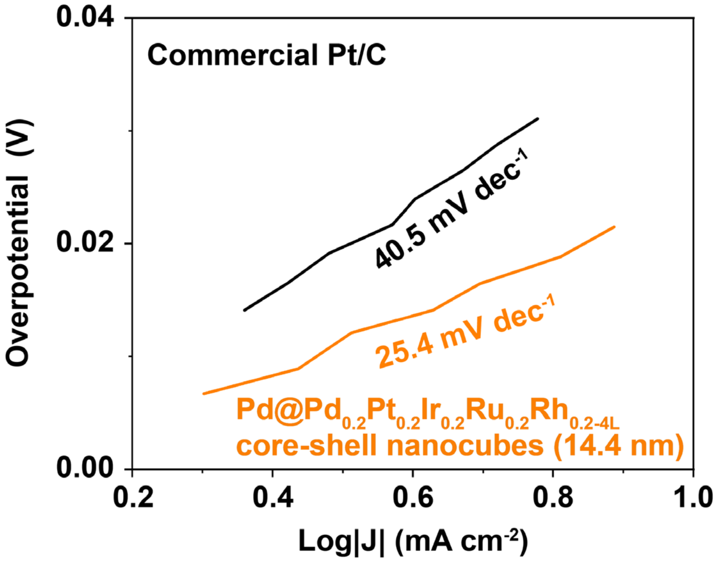

Figure S13. Tafel plots of Pd@Pd$_{0.2}$Pt$_{0.2}$Ir$_{0.2}$Ru$_{0.2}$Rh$_{0.2\text{-}4L}$ core-shell nanocubes (14.4 nm) and the commercial Pt/C samples. The analysis curves are derived from the HER polarization curves by replotting the overpotential versus the logarithm of the current density with a scan rate of 1 mV s^{-1} measured in the acidic 0.5 M H_2SO_4 electrolyte.

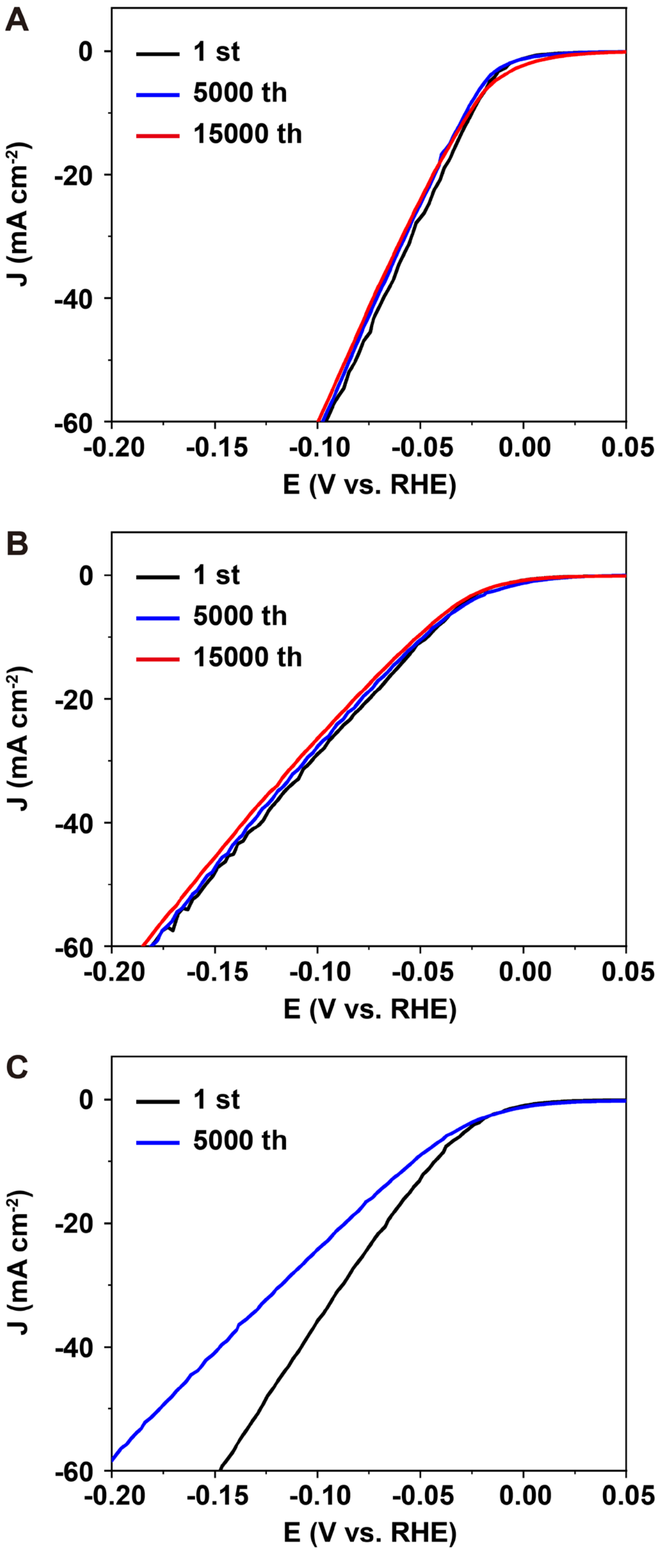

Figure S14. LSV curves before and after long-term durability tests of Pd@Pd$_{0.2}$Pt$_{0.2}$Ir$_{0.2}$Ru$_{0.2}$Rh$_{0.2}$-4L core-shell (A) cubic (14.4 nm) and (B) octahedral nanocrystals as well as (C) the commercial Pt/C samples in the acidic 0.5 M H_2SO_4 electrolyte for electrocatalytic HER.

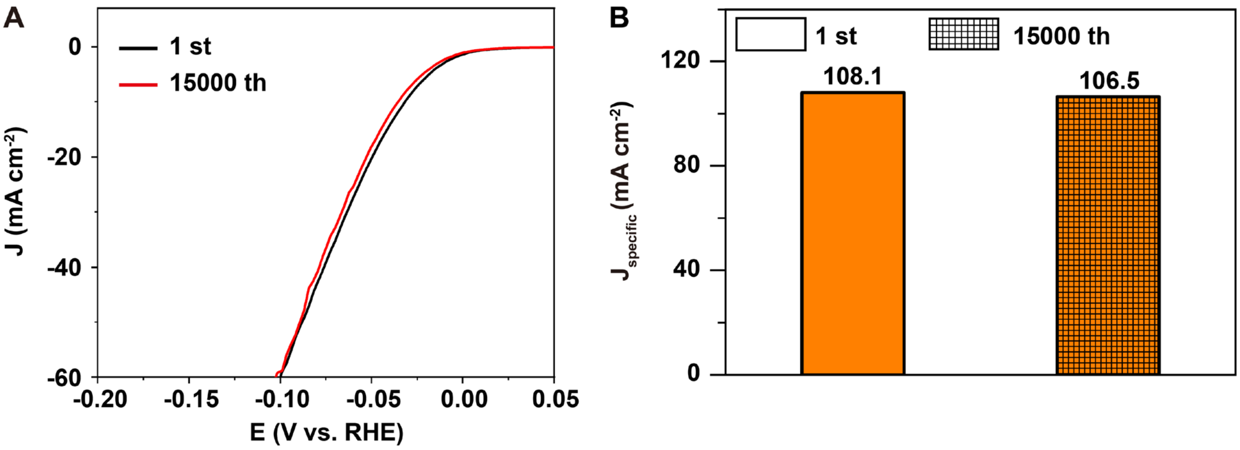

Figure S15. Long-term durability test for the representative Pd@$Pd_{0.2}Pt_{0.2}Ir_{0.2}Ru_{0.2}Rh_{0.2\text{-}4L}$ core-shell nanocubes (14.4 nm) using a graphite counter electrode in the acidic 0.5 M H_2SO_4 electrolyte for electrocatalytic HER. (A) LSV curves and (B) specific activities at -0.1 V before and after 15000 catalytic cycles, showing excellent durability. The sample preparation and the measurement method are the same as the above-mentioned process in electrocatalytic measurements for HER, except that the counter electrode was changed to a graphite electrode instead of a platinum wire to avoid the possibility of Pt oxidation and redeposition on the working electrode.

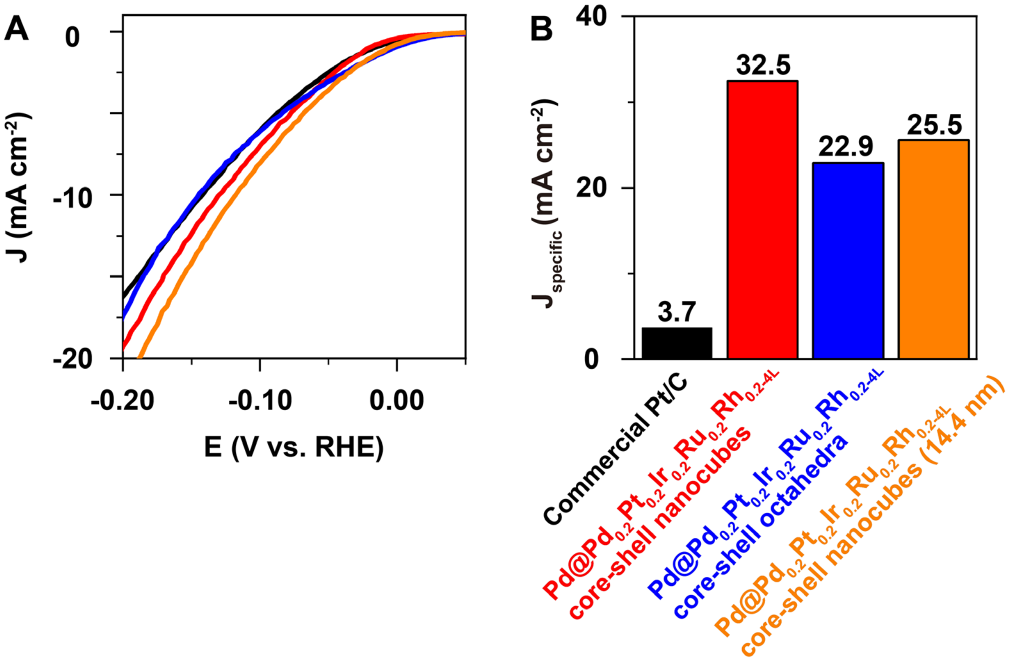

Figure S16. (A) LSV curves and (B) specific activities of Pd@Pd$_{0.2}$Pt$_{0.2}$Ir$_{0.2}$Ru$_{0.2}$Rh$_{0.2\text{-}4L}$ core-shell cubic and octahedral nanocrystals, and Pd@Pd$_{0.2}$Pt$_{0.2}$Ir$_{0.2}$Ru$_{0.2}$Rh$_{0.2\text{-}4L}$ core-shell cubic nanocrystals (14.4 nm), as well as the commercial Pt/C samples at -0.15 V versus RHE in the alkaline 1.0 M KOH electrolyte for electrocatalytic HER.

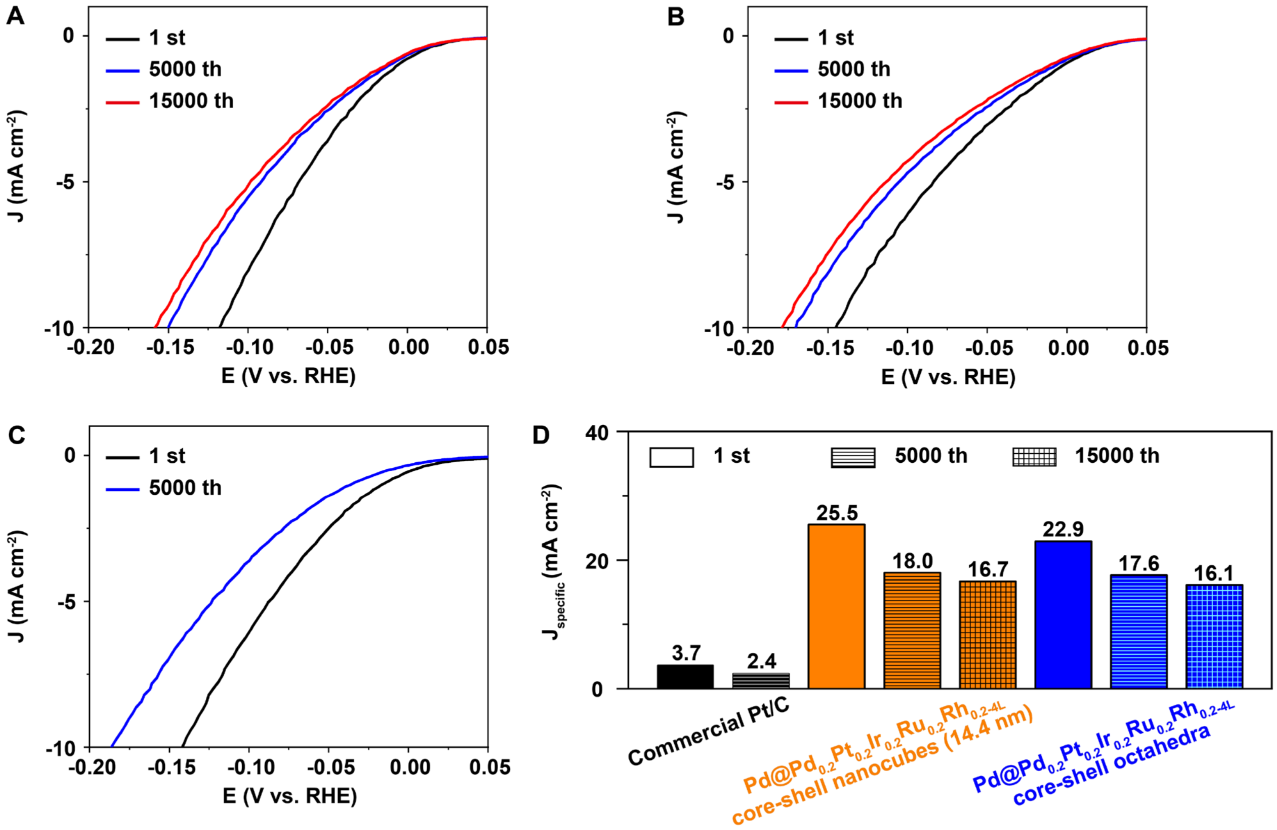

Figure S17. LSV curves before and after long-term durability tests of Pd@Pd$_{0.2}$Pt$_{0.2}$Ir$_{0.2}$Ru$_{0.2}$Rh$_{0.2\text{-}4L}$ core-shell (A) cubic (14.4 nm) and (B) octahedral nanocrystals as well as (C) the commercial Pt/C samples in the alkaline 1.0 M KOH electrolyte for electrocatalytic HER. (D) Comparisons of the specific activities at -0.15 V of these three catalysts at different cycles.

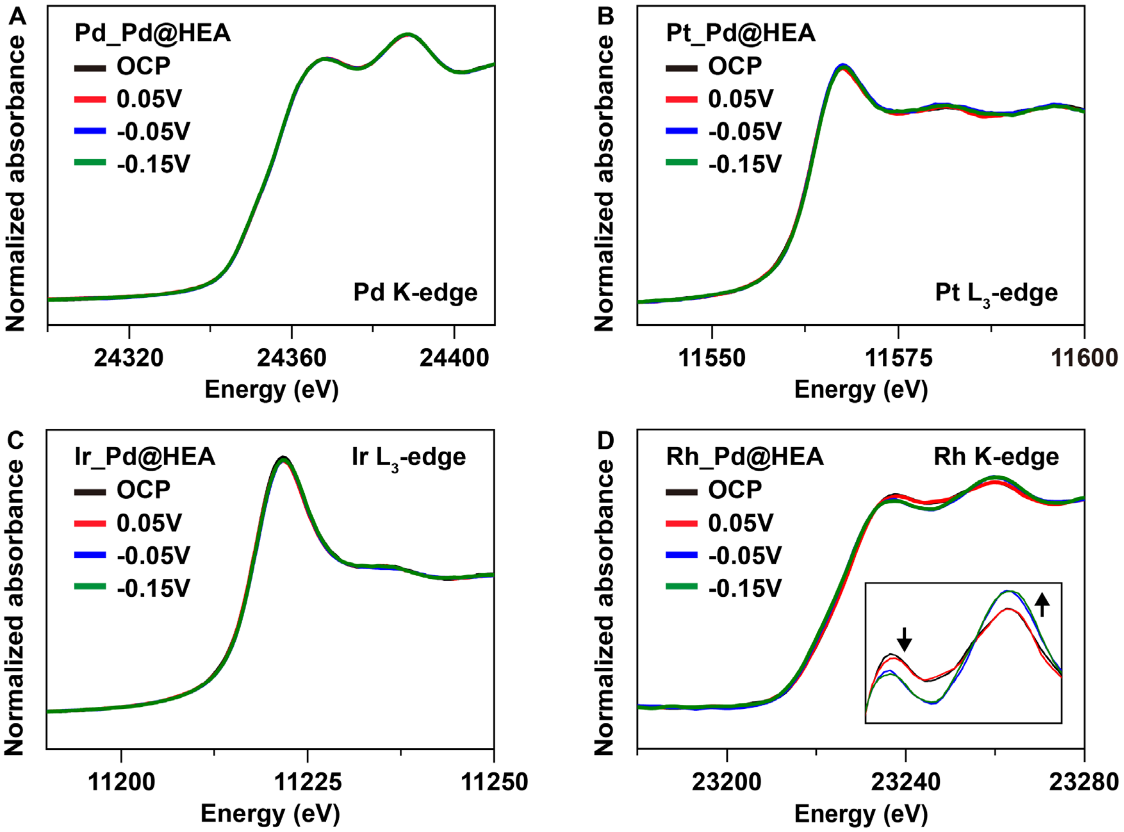

Figure S18. *In situ* XANES spectra of Pd@Pd$_{0.2}$Pt$_{0.2}$Ir$_{0.2}$Ru$_{0.2}$Rh$_{0.2\text{-}4L}$ core-shell nanocubes at the (A) Pd K-edge, (B) Pt L$_3$-edge, (C) Ir L$_3$-edge, and (D) Rh K-edge under initial condition and different applied potentials. For Rh K-edge, when the voltage shifted from cathodic to anodic, the intensity of peak at around 23237 and 23260 eV decreased and increased dramatically along with the slight shift of the absorption edge, indicating that a part of hydrogen adsorption occurred on Rh sites. Note that the spectra of Pd K-edge, Pt L$_3$-edge, and Ir L$_3$-edge for Pd@Pd$_{0.2}$Pt$_{0.2}$Ir$_{0.2}$Ru$_{0.2}$Rh$_{0.2\text{-}4L}$ core-shell nanocubes were nearly unmoved.

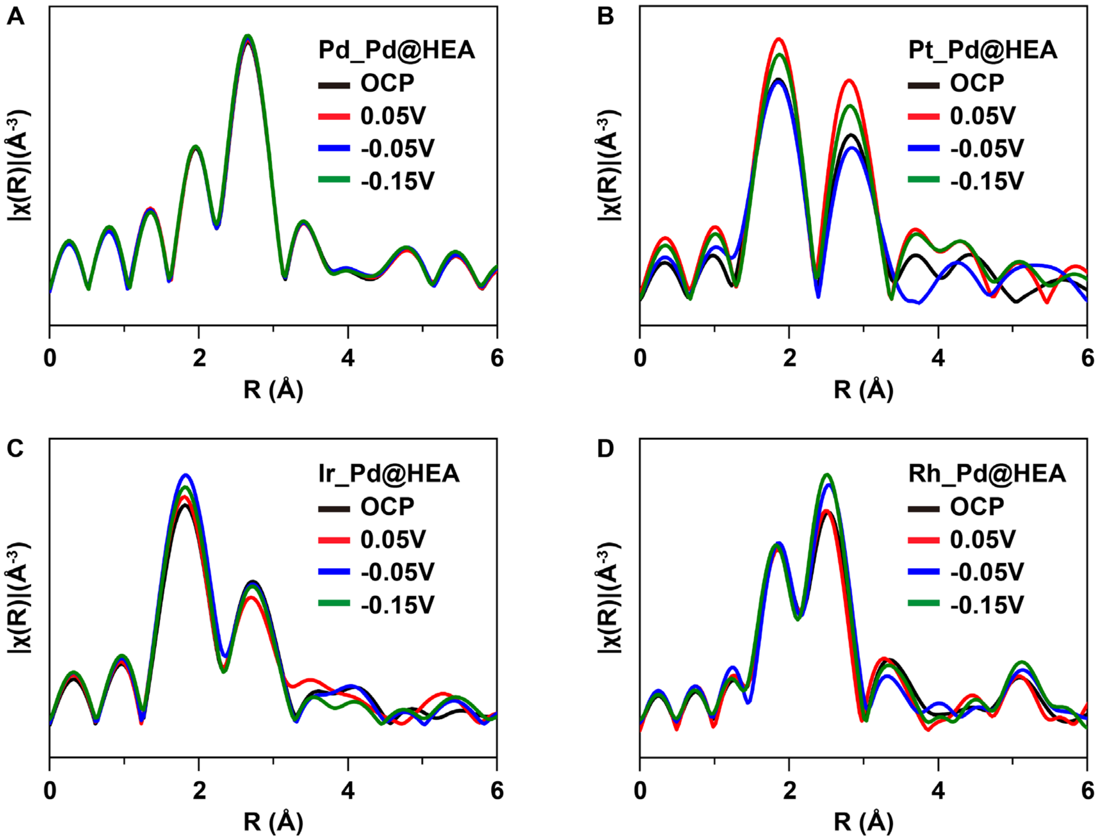

Figure S19. *In situ* FT-EXAFS spectra of Pd@$Pd_{0.2}Pt_{0.2}Ir_{0.2}Ru_{0.2}Rh_{0.2\text{-}4L}$ core-shell nanocubes at the (A) Pd K-edge, (B) Pt L_3-edge, (C) Ir L_3-edge, and (D) Rh K-edge. The average bond length for all elements in HEA remained nearly unchanged when applied to different voltages, indicating the bond structure (bond length and coordination number) did not change during the reaction. These results confirmed the structural stability of Pd@$Pd_{0.2}Pt_{0.2}Ir_{0.2}Ru_{0.2}Rh_{0.2\text{-}4L}$ core-shell nanocubes.

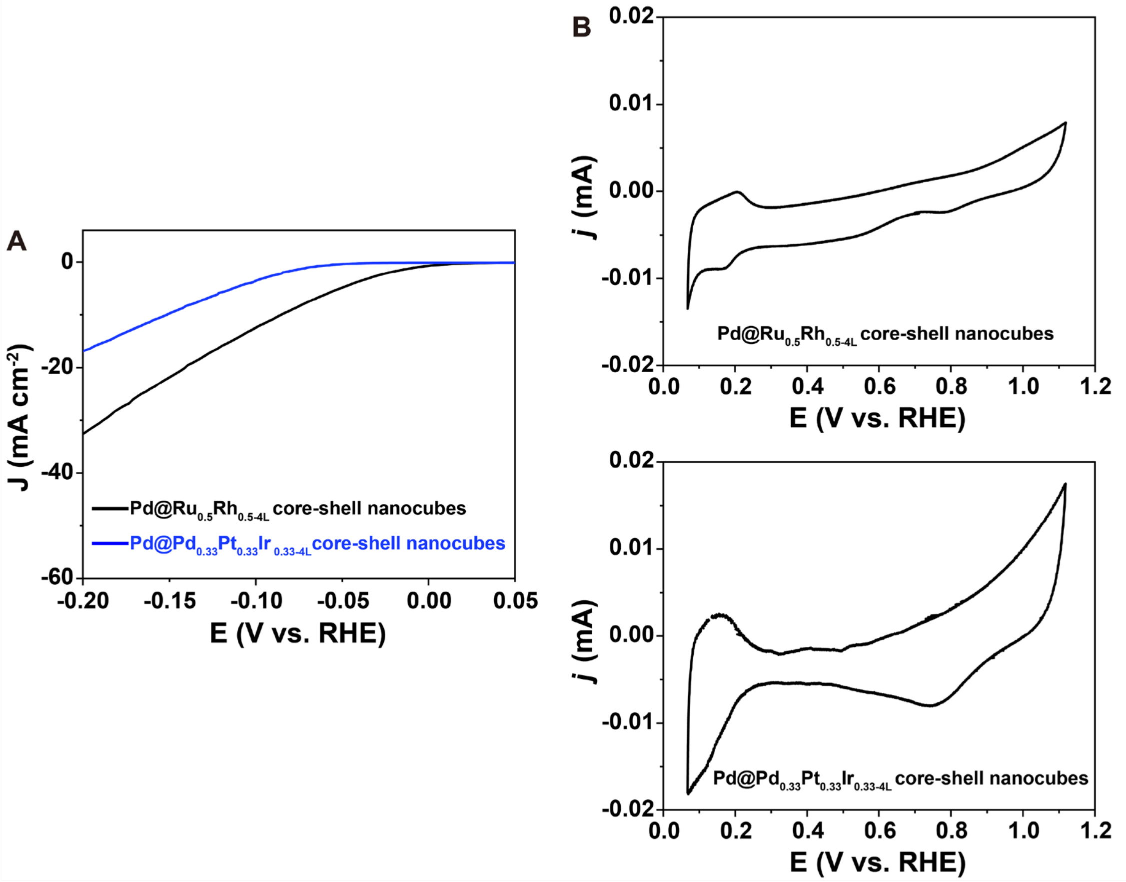

Figure S20. Electrocatalytic HER performances of bimetallic Pd@Ru$_{0.5}$Rh$_{0.5\text{-}4L}$ and trimetallic Pd@Pd$_{0.33}$Pt$_{0.33}$Ir$_{0.33\text{-}4L}$ core-shell nanocubes in the 0.5 M H_2SO_4 electrolyte. (A) LSV and (B) CV curves. Compared to the Pd@Pd$_{0.2}$Pt$_{0.2}$Ir$_{0.2}$Ru$_{0.2}$Rh$_{0.2\text{-}4L}$ core-shell nanocubes, the Pd@Ru$_{0.5}$Rh$_{0.5\text{-}4L}$ and Pd@Pd$_{0.33}$Pt$_{0.33}$Ir$_{0.33\text{-}4L}$ core-shell nanocubes showed the current density of 12.4 and 3.6 mA cm^{-2} at a specific overpotential of 0.1 V (where the current is normalized by geometric electrode area), respectively.

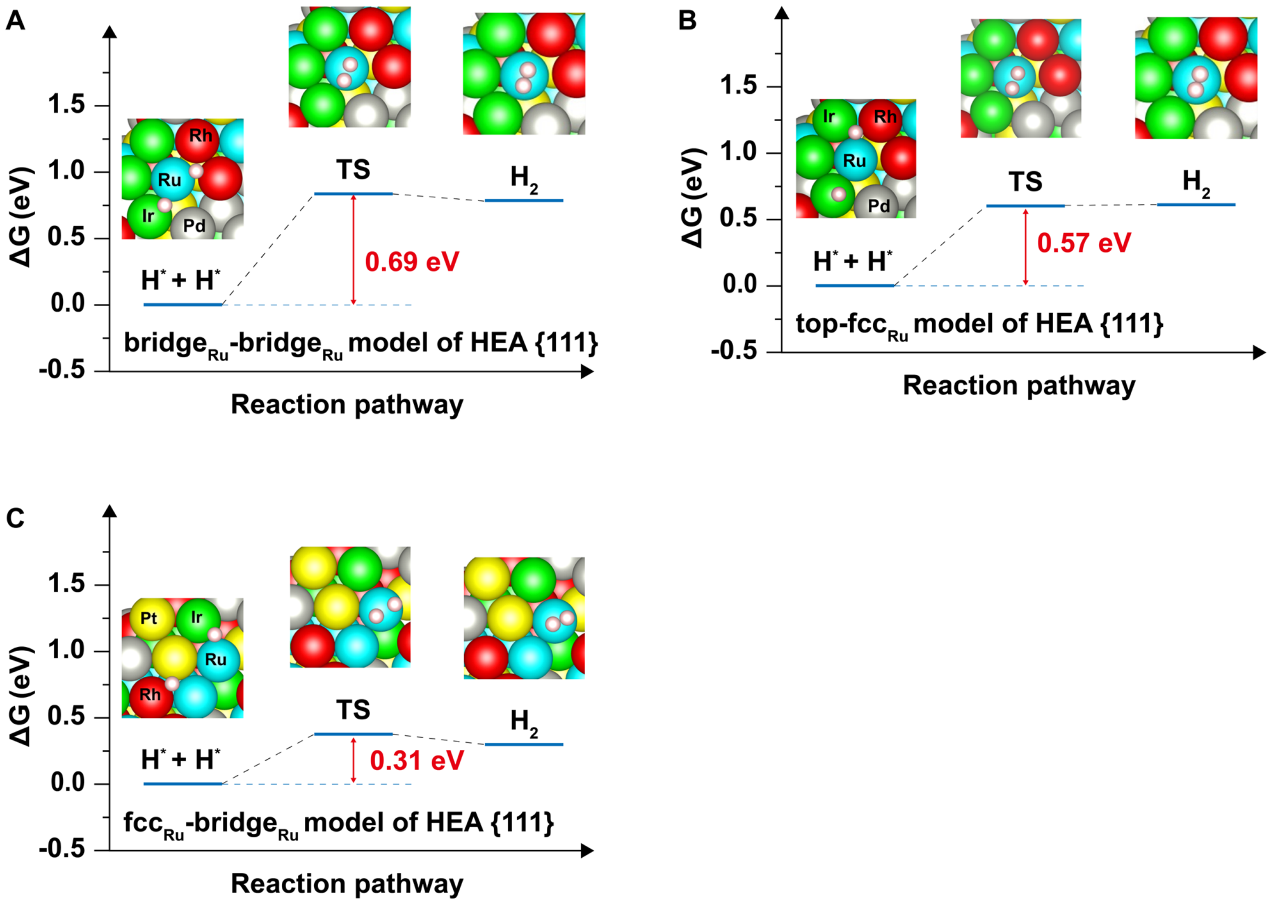

Figure S21. Free energy diagrams of the Tafel reaction paths on (A) bridge$_{\mathrm{Ru}}$-bridge$_{\mathrm{Ru}}$, (B) top-fcc$_{\mathrm{Ru}}$, and (C) fcc$_{\mathrm{Ru}}$-bridge$_{\mathrm{Ru}}$ models of HEA {111} surface.

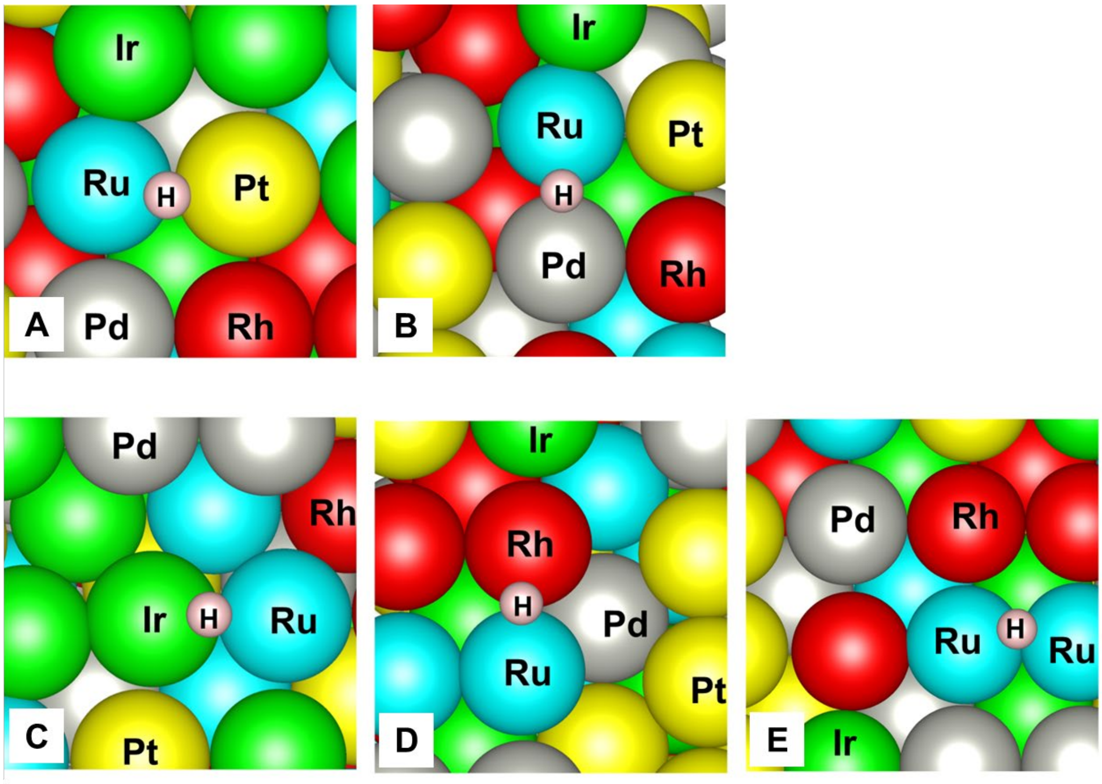

Figure S22. H adsorption on bridge$_{Ru}$ sites of HEA {100} surface. (A) Ru-Pt. (B) Ru-Pd. (C) Ru-Ir. (D) Ru-Rh. (E) Ru-Ru.

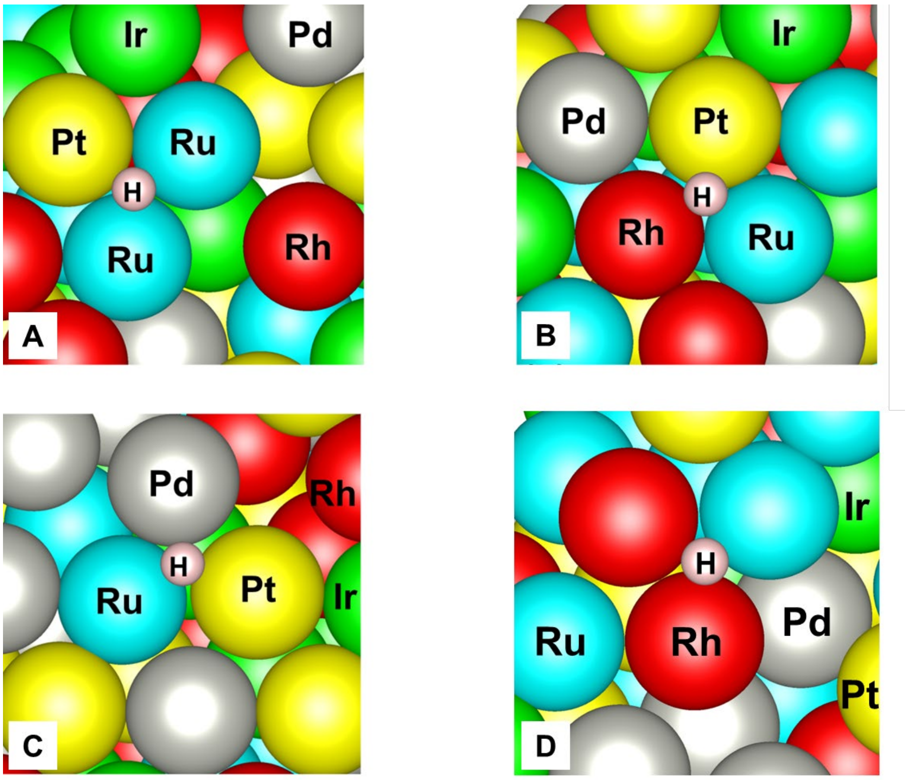

Figure S23. H adsorption on fcc$_{\mathrm{Ru}}$ sites of HEA {111} surface. (A) Pt-Ru-Ru. (B) Pt-Ru-Rh (C) Ru-Pt-Pd. (D) Ru-Rh-Rh.

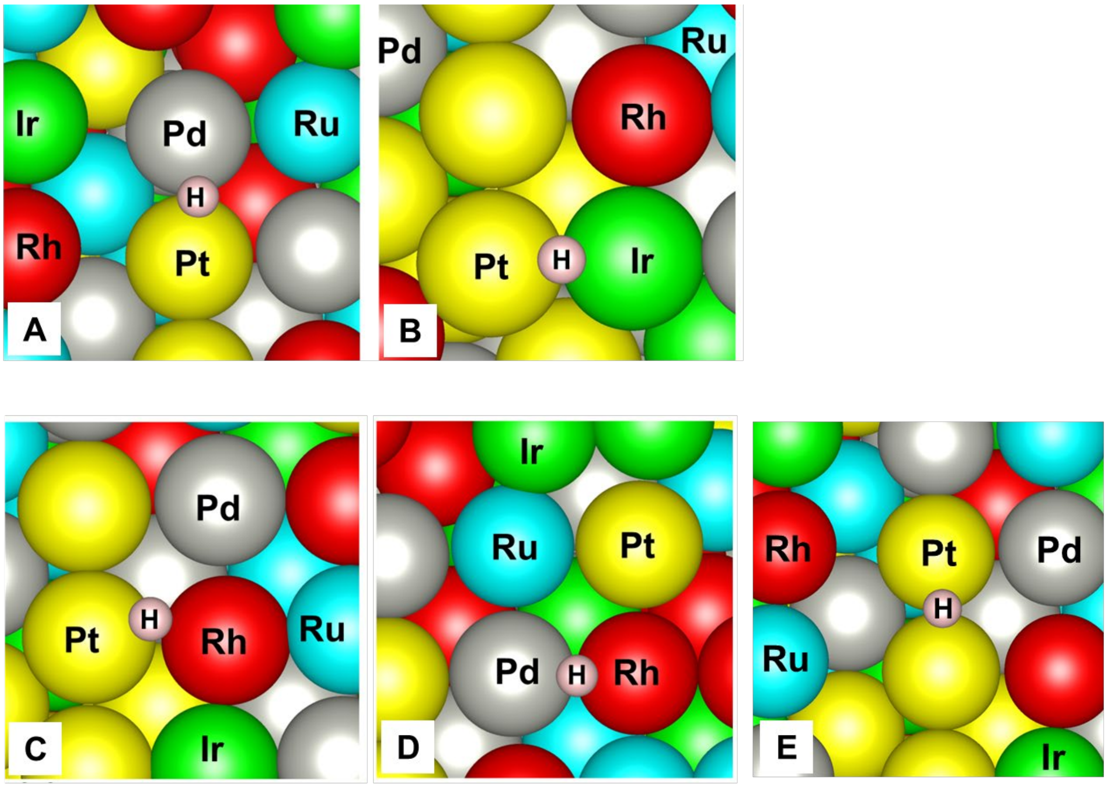

Figure S24. H adsorption on bridge sites of HEA {100} surface other than Ru sites. (A) Pt-Pd. (B) Pt-Ir. (C) Rh-Pt. (D) Pd-Rh. (E) Pt-Pt.

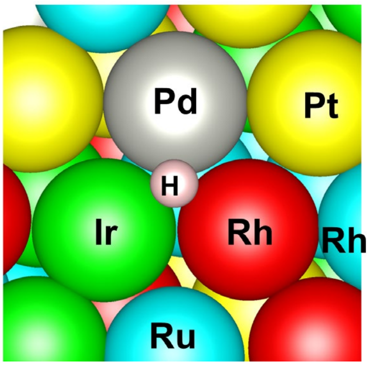

Figure S25. H adsorption on fcc sites of HEA {111} surface other than Ru sites (Ir-Pd-Rh).

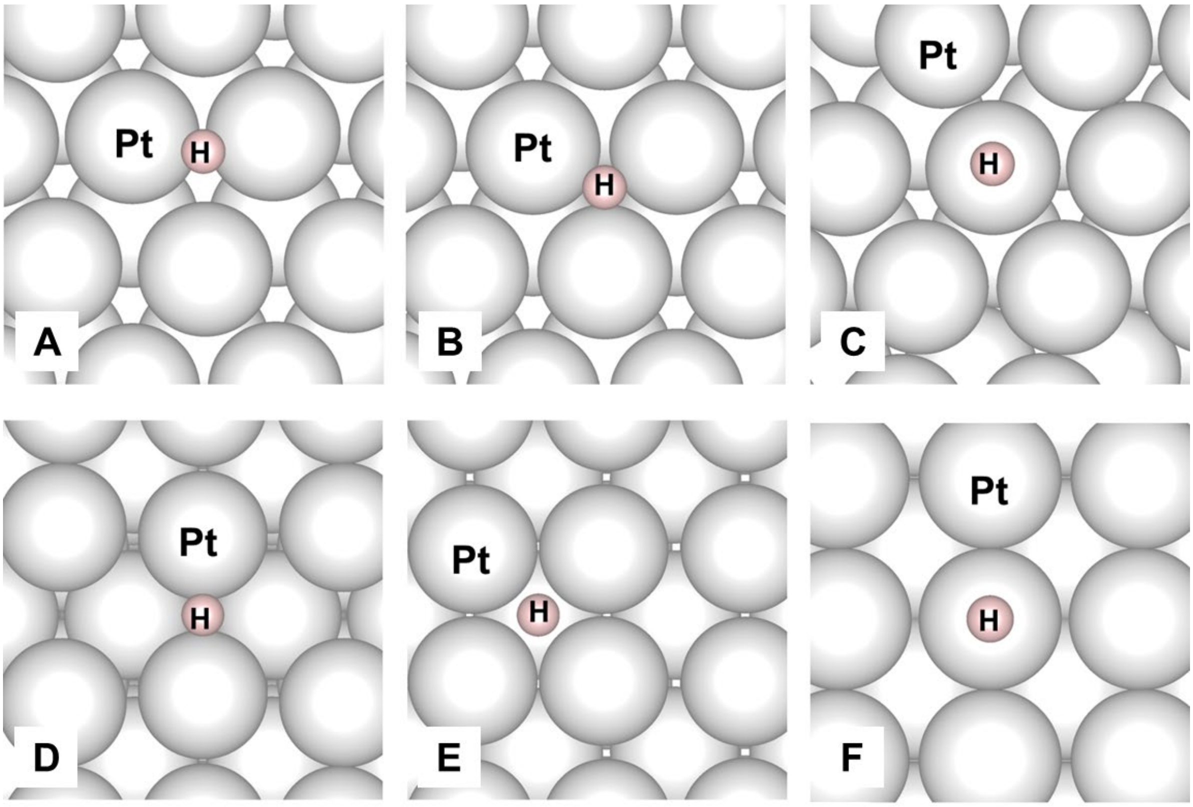

Figure S26. H adsorption on Pt surface. (A-C) H adsorption on (A) bridge, (B) fcc, and (C) top sites of Pt {111} surface. (D-F) H adsorption on (D) bridge, (E) hcp, and (F) top sites of Pt {100} surface.

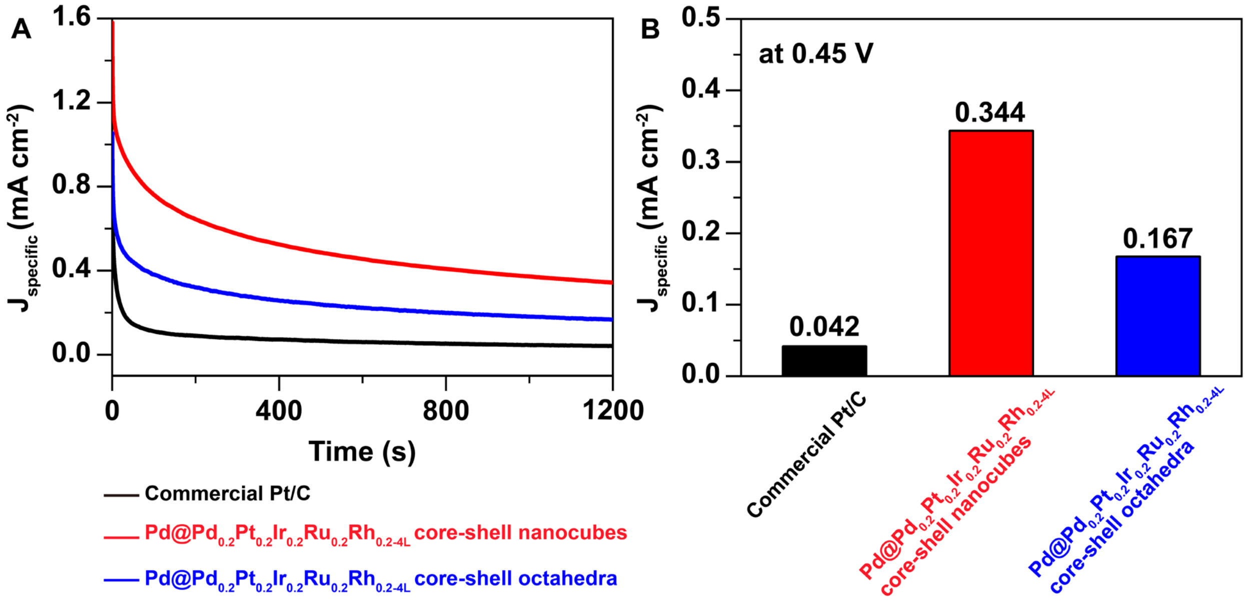

Figure S27. EOR long-term stability test in a N_2-saturated 1 M ethanol + 1 M KOH electrolyte. (A) Chronoamperometric test at a fixed potential of 0.45 V for 1200 s. (B) Comparing the steady-state current density normalized to ECSA at 1200 s. The current densities of Pd@Pd$_{0.2}$Pt$_{0.2}$Ir$_{0.2}$Ru$_{0.2}$Rh$_{0.2-4L}$ core-shell nanocubes and Pd@Pd$_{0.2}$Pt$_{0.2}$Ir$_{0.2}$Ru$_{0.2}$Rh$_{0.2-4L}$ core-shell octahedra were 8.2 times and 4.0 times higher than that of commercial Pt/C, respectively, indicating the higher durability against poisoning by catalytic intermediates.

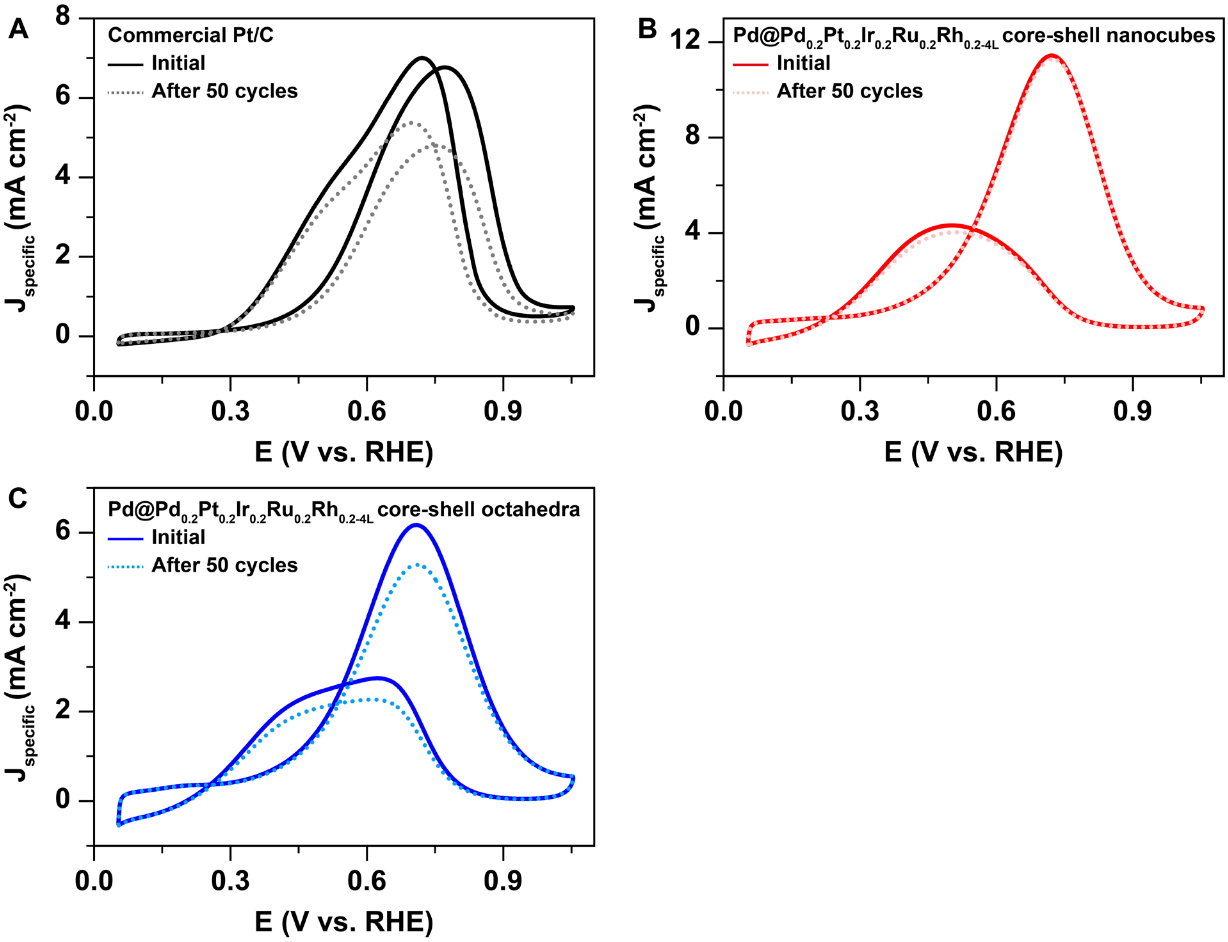

Figure S28. CV profiles for the EOR in N_2-saturated 1 M ethanol + 1 M KOH electrolyte at 1 and 50 cycles of (A) commercial Pt/C, (B) $Pd@Pd_{0.2}Pt_{0.2}Ir_{0.2}Ru_{0.2}Rh_{0.2\text{-}4L}$ core-shell nanocubes, and (C) $Pd@Pd_{0.2}Pt_{0.2}Ir_{0.2}Ru_{0.2}Rh_{0.2\text{-}4L}$ core-shell octahedra. The higher stabilities of $Pd@Pd_{0.2}Pt_{0.2}Ir_{0.2}Ru_{0.2}Rh_{0.2\text{-}4L}$ samples imply the optimal surface configurations for EOR.

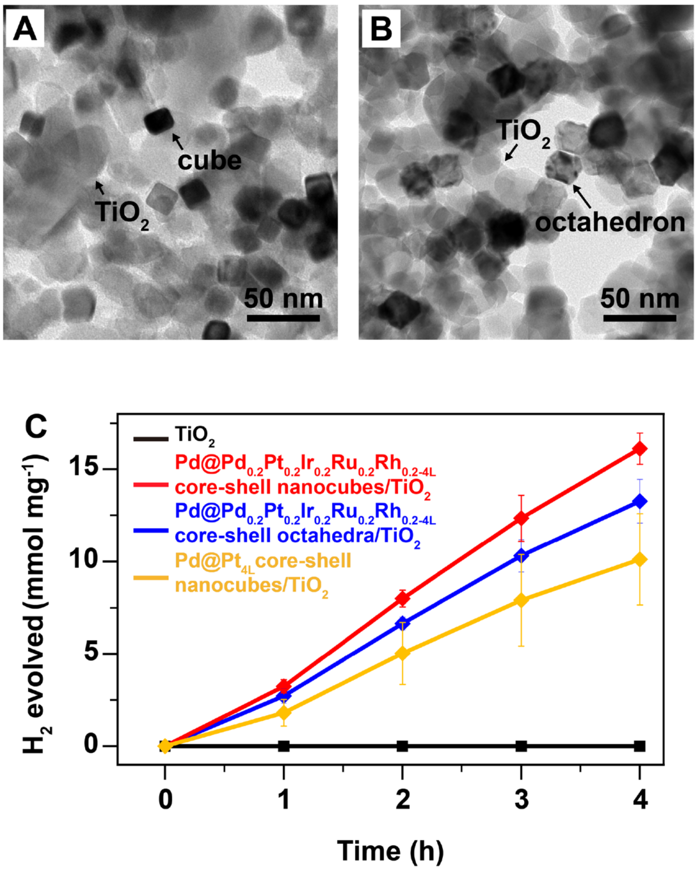

Figure S29. (A-B) TEM images of $Pd@Pd_{0.2}Pt_{0.2}Ir_{0.2}Ru_{0.2}Rh_{0.2\text{-}4L}$ core-shell (A) cubic and (B) octahedral nanocrystals loaded on commonly used TiO_2 P25 semiconductor photocatalysts. (C) Photocatalytic hydrogen evolution activities of pure TiO_2 P25, $Pd@Pd_{0.2}Pt_{0.2}Ir_{0.2}Ru_{0.2}Rh_{0.2\text{-}4L}$ core-shell nanocubes/TiO_2, $Pd@Pd_{0.2}Pt_{0.2}Ir_{0.2}Ru_{0.2}Rh_{0.2\text{-}4L}$ core-shell octahedra/TiO_2, and $Pd@Pt_{4L}$ core-shell nanocubes/TiO_2 photocatalysts over the period of 4 h.

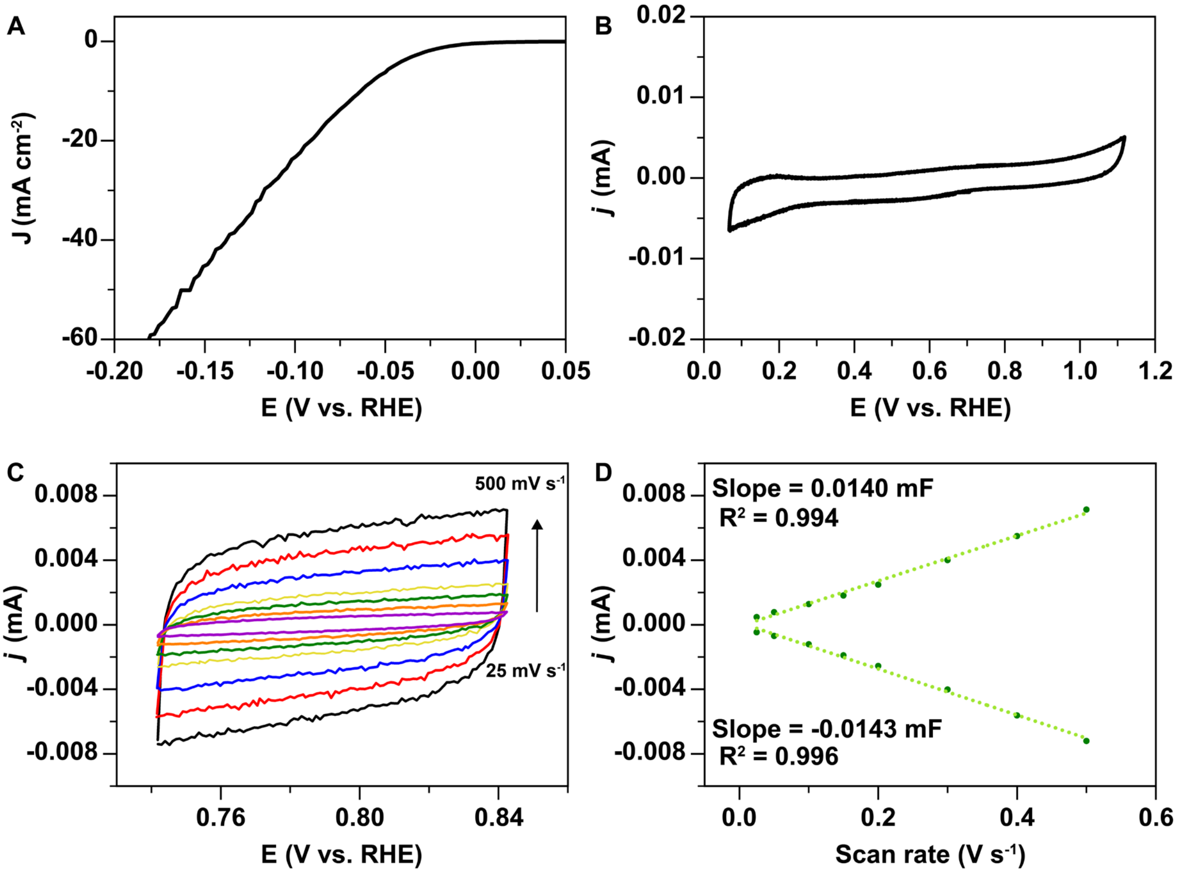

Figure S30. Electrocatalytic HER performance of $Pd@Pt_{0.2}Ir_{0.2}Co_{0.2}Fe_{0.2}Ni_{0.2\text{-}5\text{-}6L}$ core-shell nanocubes in the 0.5 M H_2SO_4 electrolyte. (A) LSV, (B) CV curves recorded between 0.05 and 1.1 V with a scan rate of 50 mV s^{-1}. (C-D) Cyclic voltammograms analysis for determining the double-layer capacitance. (C) CV curves at the scan rate from 25 mV s^{-1} to 500 mV s^{-1}, and (D) the anodic and cathodic current distribution as a function of scan rate. Due to the significant difference in the hydrogen adsorption capacity between iron-group (i.e., Co, Ni, and Fe) and platinum-group metals, using the hydrogen deposition method to estimate the ECSA of $Pd@Pt_{0.2}Ir_{0.2}Co_{0.2}Fe_{0.2}Ni_{0.2\text{-}5\text{-}6L}$ core-shell nanocubes could lead to an underestimation of the ECSA. Thus, we used C_{dl} method to estimate the ECSA of $Pd@Pt_{0.2}Ir_{0.2}Co_{0.2}Fe_{0.2}Ni_{0.2\text{-}5\text{-}6L}$ core-shell nanocubes[5,6], showing that the C_{dl} of $Pd@Pt_{0.2}Ir_{0.2}Co_{0.2}Fe_{0.2}Ni_{0.2\text{-}5\text{-}6L}$ core-shell nanocubes was 0.0142 mF. For comparison, the catalytic activity (where the current is normalized by C_{dl}) at the overpotential of 0.1 V for $Pd@Pt_{0.2}Ir_{0.2}Co_{0.2}Fe_{0.2}Ni_{0.2\text{-}5\text{-}6L}$ core-shell nanocubes was 2.6 times higher than that of commercial Pt/C with a C_{dl} value of 0.0566 mF (Figure S11).

Table S1. Synthetic strategies and catalytic applications of HEA nanocrystals in recent reports.

Materials	Methods	Crystal structures	Geometric shapes	Catalytic reactions	Ref.
PdCuAuAgBiIn	Freeze–thaw method	*fcc*	Aerogel	CO_2 reduction reaction (CO_2RR)	*Adv. Mater.* **2023**, 35, 2209242
PtIrCuNiCr, PtAuPdFeNi	Laser scanning ablation	*fcc*	Spherical particles	HER, oxygen evolution reaction (OER)	*Nat Synth.* **2023**, 1, 138−146
PtIrPdRhRuCuNiCo	Solvothermal synthesis	*fcc*	Spherical particles	--	*Chem. Mater.* **2023**, 35, 144−153
NiFeCoCuSnMo	Sparking synthesis	*fcc*	Spherical particles	Lithium–sulfur redox reaction	*Nat. Nanotechnol.* **2023**, 18, 153−159
NiPdPtRhIr	Wet-chemical synthesis	*fcc*	Spherical particles	--	Doi: 10.1021/acsnano.3c00176
IrPdPtRhRu	Wet-chemical synthesis	*fcc*	Spherical particles	HER	*J. Am. Chem. Soc.* **2022**, 144, 3365−3369
FeCoNiMnRu	Polymer nanofiber reactor	*fcc*	Spherical particles	HER, OER	*Nat. Comm.* **2022**, 13, 2662
FeCoNiCuPdIrPtAu	Fast moving bed pyrolysis	*fcc*	Spherical particles	--	*Nat. Comm.* **2022**, 13, 2789
FeCoNiSnPd	High-temperature shock	*fcc*	Spherical particles	EOR	*Adv. Funct. Mater.* **2022**, 32, 2204643
PtCoCuRuNiFe	Thermal decomposition reduction	*fcc*	Spherical particles	Methanol oxidation reaction (MOR)	*ACS Nano* **2022**, 16, 14017−14028
PdCuPtNiCo, PdCuPtNiFe	Wet-chemical synthesis and annealing	*fcc*	Spherical particles	Oxygen reduction reaction (ORR)	*ACS Nano* **2022**, 16, 18873−18885
PtPdIrRuAg	Wet-chemical synthesis	*fcc*	Subnanometer ribbons	ORR	*J. Am. Chem. Soc.* **2022**, 144, 10582−10590
IrPdPtRhRu	Continuous-flow reactor synthesis	*fcc*	Spherical particles	HER	*J. Am. Chem. Soc.* **2022**, 144, 11525−11529
PdMoGaInNi	Wet-chemical synthesis	*fcc*	Nanosheets	HER	*ACS Catal.* **2022**, 12, 11955−11959
CoNiCuRuPd	Hydrogen spillover-driven synthesis	*fcc*	Spherical particles	CO_2RR	*Nat. Comm.* **2021***,* 12, 3884
PtRuNiCoFeMo	Wet-chemical synthesis	*fcc*	Nanowires	Hydrogen oxidation reaction (HOR)	*Nat. Comm.* **2021**, 12, 6261
RuFeCoNiCu	Wet-chemical synthesis	*hcp*	Spherical particles	Nitrogen reduction reaction (N_2RR)	*Adv. Funct. Mater.* **2021**, 31, 2006939
AlPdNiCuMo	Dealloying	*fcc*	Nanoporous HEA	EOR	*Adv. Funct. Mater.* **2021**, 31, 2007129
PtPdFeCoNi	Microwave heating	*fcc*	Spherical particles	--	*ACS Nano* **2021**, 15, 14928−14937
NiCoFePtRh	Co-reduction and annealing	*fcc*	Spherical particles	HER	*J. Am. Chem. Soc.* **2021**, 143, 17117−17127
PtNiFeCoCu	Wet-chemical synthesis	*fcc*	Spherical particles	HER, MOR	*Nat. Comm.* **2020**, 11, 5437

RuIrFeCoNi	Droplet-to-particle	*fcc*	Hollow spherical particles	ORR, OER	*Adv. Mater.* **2020**, 32, 2002853
FeCoNiCuPt, FeCoNiPdPt, FeCoNiCuPd	Aerosol synthesis	*fcc*	Spherical particles	--	*Langmuir* **2020**, 36, 1985−1992
RuRhPdOsIrPt	Wet-chemical synthesis	*fcc*	Spherical particles	EOR	*J. Am. Chem. Soc.* **2020**, 142, 13833−13838
AuAgPtPdCu	Melting and cryogrinding	*fcc*	Spherical particles	CO_2RR	*ACS. Catal.* **2020**, 10, 3658−3663
PdIrPtRhRu	Solvothermal synthesis	*fcc*	Spherical particles	--	*Angew. Chem. Int. Ed.* **2020**, 59, 21920−21924
CoFeLaNiPt	Nanodroplet-mediated electrodeposition	*amorphous*	Irregular particle	HER, OER	*Nat Commun.* **2019**, 10, 2650
CoMoFeNiCu	Carbothermal shock	*fcc*	Spherical particles	NH_3 decomposition	*Nat. Comm.* **2019,** 10, 4011
PtPdCoNiFeAuCuSn	Carbothermal shock	*fcc*	Spherical particles	NH_3 oxidation	*Science*, **2018**, 359, 1489−1494
FeCoPdIrPt	Fast-moving bed pyrolysis	*fcc*	Spherical particles	HER	*Nat. Comm.* **2016 (2020)**, 11 Doi: 10.1038/s41467-020-15934-1

Table S2. Reduction potentials of the metal salt precursors and crystal structures of the metals.[7,8]

[a]Standard conditions: 25 °C and 1 atm. SHE: standard hydrogen electrode.

Reduction reaction	E_0 (V vs SHE)[a]	Metal	Crystal lattice	Lattice constant (Å)
$Au^{3+} + 3e^- \rightarrow Au$	1.50	Au	*fcc*	4.08
$Pt^{2+} + 2e^- \rightarrow Pt$	1.18	Pt	*fcc*	3.92
$Ir^{3+} + 3e^- \rightarrow Ir$	1.16	Ir	*fcc*	3.84
$Pd^{2+} + 2e^- \rightarrow Pd$	0.95	Pd	*fcc*	3.89
$Os^{4+} + 4e^- \rightarrow Os$	0.85	Os	*hcp*	a = 2.73 c = 4.32
$Rh^{3+} + 3e^- \rightarrow Rh$	0.76	Rh	*fcc*	3.80
$Ru^{3+} + 3e^- \rightarrow Ru$	0.45	Ru	*hcp*	a = 2.71, c = 4.28
$Ni^{2+} + 2e^- \rightarrow Ni$	-0.25	Ni	*fcc*	3.52
$Co^{2+} + 2e^- \rightarrow Co$	-0.28	Co	*hcp*	a = 2.51, c = 4.07
$Fe^{2+} + 2e^- \rightarrow Fe$	-0.44	Fe	*bcc*	2.87

Table S3. ICP-OES results of the atomic compositions of shells in the core-shell nanocrystals obtained in this work.

	Composition of shell (at %)						
Sample name	Pt	Pd	Ir	Ru	Rh	Os	Au
Pd@Pd$_{0.2}$Pt$_{0.2}$Ir$_{0.2}$Ru$_{0.2}$Rh$_{0.2\text{-}2L}$ core-shell nanocubes	19.7	21.9	17.9	18.5	22.0	--	--
Pd@Pd$_{0.2}$Pt$_{0.2}$Ir$_{0.2}$Ru$_{0.2}$Rh$_{0.2\text{-}4L}$ core-shell nanocubes	22.3	18.2	19.3	19.6	20.7	--	--
Pd@Pd$_{0.2}$Pt$_{0.2}$Ir$_{0.2}$Ru$_{0.2}$Rh$_{0.2\text{-}6L}$ core-shell nanocubes	21.2	20.3	20.0	18.9	19.6	--	--
Pd@Pd$_{0.2}$Pt$_{0.2}$Ir$_{0.2}$Ru$_{0.2}$Rh$_{0.2\text{-}4L}$ core-shell octahedra	22.4	17.6	19.1	19.9	21.0	--	--
Pd@Pd$_{0.2}$Pt$_{0.2}$Ir$_{0.2}$Ru$_{0.2}$Rh$_{0.2\text{-}4L}$ core-shell nanocubes (14.4 nm)	22.3	18.4	19.1	19.6	20.6	--	--
Pd@Pt$_{0.33}$Ir$_{0.33}$Ru$_{0.33\text{-}6L}$ core-shell nanocubes	36.3	--	31.3	32.4	--	--	--
Pd@Pt$_{0.25}$Ir$_{0.25}$Ru$_{0.25}$Rh$_{0.25\text{-}6L}$ core-shell nanocubes	27.3	--	23.7	23.8	25.3	--	--
Pd@Pt$_{0.2}$Ir$_{0.2}$Ru$_{0.2}$Rh$_{0.2}$Au$_{0.2\text{-}7L}$ core-shell nanocubes	21.5	--	19.8	21.4	22.4	--	14.8
Pd@Pd$_{0.17}$Pt$_{0.17}$Ir$_{0.17}$Ru$_{0.17}$Rh$_{0.17}$Au$_{0.17\text{-}7L}$ core-shell nanocubes	17.7	17.7	16.3	17.7	18.5	--	12.1
Pd@Pd$_{0.14}$Pt$_{0.14}$Ir$_{0.14}$Ru$_{0.14}$Rh$_{0.14}$Os$_{0.14}$Au$_{0.14\text{-}7L}$ core-shell nanocubes	16.2	10.1	15.1	15.3	17.4	13.9	12.1
Pd@Pd$_{0.225}$Pt$_{0.1}$Ir$_{0.225}$Ru$_{0.225}$Rh$_{0.225\text{-}4L}$ core-shell nanocubes	11.1	23.5	21.0	21.5	22.9	--	--
Pd@Pd$_{0.175}$Pt$_{0.3}$Ir$_{0.175}$Ru$_{0.175}$Rh$_{0.175\text{-}4L}$ core-shell nanocubes	32.7	15.0	16.9	17.4	18.1	--	--
Pd@Pd$_{0.15}$Pt$_{0.4}$Ir$_{0.15}$Ru$_{0.15}$Rh$_{0.15\text{-}4L}$ core-shell nanocubes	39.9	16.9	13.5	13.9	15.9	--	--
Pd@Pd$_{0.125}$Pt$_{0.5}$Ir$_{0.125}$Ru$_{0.125}$Rh$_{0.125\text{-}4L}$ core-shell nanocubes	50.3	12.4	11.5	11.8	13.9	--	--
Pd@Pd$_{0.1}$Pt$_{0.6}$Ir$_{0.1}$Ru$_{0.1}$Rh$_{0.1\text{-}4L}$ core-shell nanocubes	59.6	9.9	9.3	9.6	11.7	--	--
Pd@Pt$_{0.2}$Ir$_{0.2}$Co$_{0.2}$Fe$_{0.2}$Ni$_{0.2\text{-}5\text{-}6L}$ core-shell nanocubes	Co	Fe	Ni	Pt	Ir		
	27.8	22.2	20.1	21.6	11.0		
Pd@Pd$_{0.1}$Pt$_{0.1}$Ir$_{0.1}$Ru$_{0.1}$Rh$_{0.1}$Os$_{0.1}$Au$_{0.1}$Co$_{0.1}$Fe$_{0.1}$Ni$_{0.1\text{-}6L}$ core-shell nanocubes	Co	Fe	Ni	Pt	Pd	Ir	Ru
	3.4	10.6	15.4	7.7	9.9	12.6	9.3
	Rh	Os	Au				
	10.1	9.9	11.0				
	Total composition (at%)						
Sample name	Pt	Pd	Ir	Ru	Rh		
Pd$_{0.2}$Pt$_{0.2}$Ir$_{0.2}$Ru$_{0.2}$Rh$_{0.2}$ hollow nanocages	19.4	28.0	14.3	21.3	17.0		

Table S4. Average atomic layers (n) of shell calculated from the ICP-OES data for the Pd, Pt, Ir, Ru, Rh, Os, Au, Co, Fe, and Ni contents in the core-shell nanocrystals; the atomic percentage (at %) of shell calculated from the atomic layers (n) and the size of Pd seeds with cubic and octahedral shapes; and the at % of shell calculated from the ICP-OES data.

Sample name	n atomic layers	at % of shell derived from calculation	at % of shell derived from ICP-OES data
Pd@Pd$_{0.2}$Pt$_{0.2}$Ir$_{0.2}$Ru$_{0.2}$Rh$_{0.2\text{-}2L}$ core-shell nanocubes	2	10.9%	11.2%
Pd@Pd$_{0.2}$Pt$_{0.2}$Ir$_{0.2}$Ru$_{0.2}$Rh$_{0.2\text{-}4L}$ core-shell nanocubes	4	20.4%	19.9%
Pd@Pd$_{0.2}$Pt$_{0.2}$Ir$_{0.2}$Ru$_{0.2}$Rh$_{0.2\text{-}6L}$ core-shell nanocubes	6	28.6%	29.9%
Pd@Pd$_{0.2}$Pt$_{0.2}$Ir$_{0.2}$Ru$_{0.2}$Rh$_{0.2\text{-}4L}$ core-shell octahedra	4	22.9%	20.8%
Pd@Pd$_{0.2}$Pt$_{0.2}$Ir$_{0.2}$Ru$_{0.2}$Rh$_{0.2\text{-}4L}$ core-shell nanocubes (14.4 nm)	4	27.4%	27.2%
Pd@Pt$_{0.33}$Ir$_{0.33}$Ru$_{0.33\text{-}6L}$ core-shell nanocubes	6	28.6%	29.5%
Pd@Pt$_{0.25}$Ir$_{0.25}$Ru$_{0.25}$Rh$_{0.25\text{-}6L}$ core-shell nanocubes	6	28.6%	29.3%
Pd@Pt$_{0.2}$Ir$_{0.2}$Ru$_{0.2}$Rh$_{0.2}$Au$_{0.2\text{-}7L}$ core-shell nanocubes	7	32.4%	33.9%
Pd@Pt$_{0.2}$Ir$_{0.2}$Co$_{0.2}$Fe$_{0.2}$Ni$_{0.2\text{-}5\text{-}6L}$ core-shell nanocubes	5-6	24.6% (5L) 28.6% (6L)	26.5%
Pd@Pd$_{0.17}$Pt$_{0.17}$Ir$_{0.17}$Ru$_{0.17}$Rh$_{0.17}$Au$_{0.17\text{-}7L}$ core-shell nanocubes	7	32.4%	33.9%
Pd@Pd$_{0.14}$Pt$_{0.14}$Ir$_{0.14}$Ru$_{0.14}$Rh$_{0.14}$Os$_{0.14}$Au$_{0.14\text{-}7L}$ core-shell nanocubes	7	32.4%	31.9%
Pd@Pd$_{0.1}$Pt$_{0.1}$Ir$_{0.1}$Ru$_{0.1}$Rh$_{0.1}$Os$_{0.1}$Au$_{0.1}$Co$_{0.1}$Fe$_{0.1}$Ni$_{0.1\text{-}6L}$ core-shell nanocubes	6	28.6%	29.6%
Pd@Pd$_{0.225}$Pt$_{0.1}$Ir$_{0.225}$Ru$_{0.225}$Rh$_{0.225\text{-}4L}$ core-shell nanocubes	4	20.4%	20.3%
Pd@Pd$_{0.175}$Pt$_{0.3}$Ir$_{0.175}$Ru$_{0.175}$Rh$_{0.175\text{-}4L}$ core-shell nanocubes	4	20.4%	19.9%
Pd@Pd$_{0.15}$Pt$_{0.4}$Ir$_{0.15}$Ru$_{0.15}$Rh$_{0.15\text{-}4L}$ core-shell nanocubes	4	20.4%	17.6%
Pd@Pd$_{0.125}$Pt$_{0.5}$Ir$_{0.125}$Ru$_{0.125}$Rh$_{0.125\text{-}4L}$ core-shell nanocubes	4	20.4%	19.9%
Pd@Pd$_{0.1}$Pt$_{0.6}$Ir$_{0.1}$Ru$_{0.1}$Rh$_{0.1\text{-}4L}$ core-shell nanocubes	4	20.4%	19.7%
Pd@Pt$_{4L}$ core-shell nanocubes	4	20.4%	21.8%
Pd@Pd$_{4L}$ core-shell nanocubes	4	20.4%	20.4%
Pd@Ir$_{4L}$ core-shell nanocubes	4	20.4%	19.3%
Pd@Ru$_{4L}$ core-shell nanocubes	4	20.4%	20.0%
Pd@Rh$_{4L}$ core-shell nanocubes	4	20.4%	21.3%

Table S5. The binding energy of each element in the core-level XPS analysis of $Pd@Pd_{0.2}Pt_{0.2}Ir_{0.2}Ru_{0.2}Rh_{0.2\text{-}4L}$ core-shell nanocubes (Figure 2A and B) and octahedra (Figure S5) along with the table lookup values. (Note: Table lookup values are from the *Handbook of X-ray Photoelectron Spectroscopy.* J. F. Modulder, W. F. Stickle, P. E. Sobol, K. D. Bomben. Perkin-Elmer Corp. 1992)

Sample	Ru $3d_{5/2}$	Rh $3d_{5/2}$	Pd3 $d_{5/2}$	Ir $4f_{7/2}$	Pt $4f_{7/2}$
Table lookup value	**280.1**	**307.0**	**335.1**	**60.9**	**71.2**
$Pd@Pd_{0.2}Pt_{0.2}Ir_{0.2}Ru_{0.2}Rh_{0.2\text{-}4L}$ core-shell nanocubes	280	307.1	335.3	60.5	71.3
$Pd@Pd_{0.2}Pt_{0.2}Ir_{0.2}Ru_{0.2}Rh_{0.2\text{-}4L}$ core-shell octahedra	280.1	307.0	335.1	60.6	70.9

Table S6. Comparison of the specific activities of facet-controlled Pd@HEA nanocrystals obtained in this work with other advanced noble metal catalysts reported previously toward HER in the acidic 0.5 M H_2SO_4 electrolyte.

Composition	Catalyst loading (mg $cm^{-2}{}_{geo}$)	η (mV) for 10 mA cm^{-2}	TOFs (at x overpotential) (s^{-1})	Ref.
$Al_{87}Ag_1Au_1Co_1Cu_1Fe_1Ir_1Mo_1Ni_1Pd_1Pt_1Rh_1Ru_1Ti_1$ (np-UHEAs)	~0.25	32	--	*Chem. Sci.* **2021**, 12, 11306−11315
PtRuRhCoNi NWs	0.0142	13	31.9@50 mV	*Appl. Catal. B* **2022**, 312, 121431
Co−Fe−Ni−Pt−Ta−vxc72	0.349	10.6	--	*ACS Appl. Nano Mater.* **2022**, 5, 9810−9817
NiCoFePtRh (us-HEA/C)	0.0018	27	11.0@25 mV (Only consider Pt, Rh sites)	*J. Am. Chem. Soc.* **2021**, 143, 17117−17127
PdMnCo/NC-2	0.285	34	--	*ACS Appl. Mater. Interfaces* **2017**, 9, 38419−38427
Pt-Ru dual-metal dimers	0.00167	14.4	--	*Nat. Commun.* **2019**, 10, 4936
PtRu@RFCS	0.0184	19.7	4.03@100 mV	*Energy Environ. Sci.* **2018**, 11, 1232−1239
Ru/MeOH/THF	35.21	83	0.87@100 mV	*Chem. Commun.* **2017**, 53, 11713−11716
$RuIrO_x$	0.01	12	--	*Nat. Commun.* **2019**, 10, 4875
$Ru@C_2N$	0.0818	13.5	0.67@25 mV 1.95@50 mV	*Nat. Nanotechnol.* **2017**, 12, 441−446
PdCu@Pd NCs	0.14 (87.65 μg_{Pd} cm^{-2})	65	1.53@0 mV	*ACS Appl. Mater. Interfaces* **2017**, 9, 8151−8160
Ir@CON	0.1025	13.6	0.66@25 mV	*Adv. Mater.* **2018**, 30, 1805606
Ru@NG	0.2014	42.7	0.042@25 mV 0.144@50 mV 0.519@100 mV	*J. Mater. Chem. A* **2018**, 6, 13859−13866
Pt@PCM	0.0112	105	43.6@500 mV	*Sci. Adv.*, **2018**, 4, eaao6657.
Pt/Si	0.0358	46	25.7@50 mV	*Adv. Mater.* **2020**, 32, 1906384
$Pt_{81}Fe_{28}Co_{10}$	0.0449	~20		*Adv Mater.* **2016**, 28, 2077−2084
$Ni_{43}Ru_{57}$ nanoalloy	0.1678	41		*ACS Appl. Mater. Interfaces* **2017**, 9, 17326−17336
Ru/NG-750	0.0242	53	0.04@100 mV	*ACS Appl. Mater. Interfaces* **2017**, 9,

				3785−3791
Pd@PdPt	0.566	39	--	*J. Mater. Chem. A*. **2016**, 4, 16690−16697
NiAu/Au	0.2037	50	--	*J Am Chem Soc*. **2015**, 137, 5859−5862
Pt-Cu/CNFs-1:2	--	71	--	*Adv. Mater. Interfaces* **2017**, 4, 1700005
IrHNC	0.25	4.5	4.21@25 mV	*Nat. Commun.* **2019**, 10, 4060
Pt$_1$/OLC	0.0014	38	40.78@100 mV	*Nat. Energy.* **2019**, 4, 512−518
1% PtW$_6$O$_{24}$/C	--	22	33.35@100 mV	*Nat. Commun.* **2020**, 11, 490
Pd@Pd$_{0.2}$Pt$_{0.2}$Ir$_{0.2}$Ru$_{0.2}$Rh$_{0.2\text{-}4L}$ core-shell nanocubes (14.4 nm) enclosed by {100} facets	0.0101	24.9	7.9@25 mV 21.3@50mV 49.3@100 mV	This work
Pd@Pd$_{0.2}$Pt$_{0.2}$Ir$_{0.2}$Ru$_{0.2}$Rh$_{0.2\text{-}4L}$ core-shell nanocubes enclosed by {100} facets	0.0101	41.9	3.9@25 mV 14.8@50 mV 44.6@100 mV	This work
Pd@Pd$_{0.2}$Pt$_{0.2}$Ir$_{0.2}$Ru$_{0.2}$Rh$_{0.2\text{-}4L}$ core-shell octahedra enclosed by {111} facets	0.0101	46.6	3.4@25 mV 10.5@50 mV 28.1@100 mV	This work

Table S7. The calculated reaction barriers of the Tafel step of HER on the twelve representative Ru sites of the {100} and {111} surfaces of $Pd@Pd_{0.2}Pt_{0.2}Ir_{0.2}Ru_{0.2}Rh_{0.2\text{-}4L}$ core-shell nanocubes and octahedra, respectively. The possible reaction mechanisms regarding the adsorption sites of H* are considered for each facet, including bridge-bridge, top-top, hcp-hcp, bridge-top, hcp-top, and hcp-bridge for HEA {100} and bridge-bridge, top-top, fcc-fcc, bridge-top, top-fcc, and fcc-bridge for HEA {111}.

{100}	Energy barrier	Fig.	{111}	Energy barrier	Fig.
$bridge_{Ru}$-$bridge_{Ru}$	0.20 eV	4 F	$bridge_{Ru}$-$bridge_{Ru}$	0.69 eV	S21 A
top-top (H_2 formation on Ru)	NA		top-top	NA	
hcp_{Ru}-hcp_{Ru}	NA		fcc_{Ru}-fcc_{Ru}	NA	
top-$bridge_{Ru}$	NA		top-$bridge_{Ru}$	NA	
hcp_{Ru}-top	NA		top-fcc_{Ru}	0.57 eV	S21 B
hcp_{Ru}-$bridge_{Ru}$	NA		fcc_{Ru}-$bridge_{Ru}$	0.31 eV	S21 C

Note: NA mean not available, H cannot stabilize on these sites.

Table S8. Adsorption energy (ΔH) and free energy (ΔG) of H adsorption on the representative Ru sites and extra possible sites of the {100} and {111} surfaces of Pd@Pd$_{0.2}$Pt$_{0.2}$Ir$_{0.2}$Ru$_{0.2}$Rh$_{0.2\text{-}4L}$ core-shell nanocubes and octahedra, respectively. It can be seen that the Ru sites of both Pd@Pd$_{0.2}$Pt$_{0.2}$Ir$_{0.2}$Ru$_{0.2}$Rh$_{0.2\text{-}4L}$ core-shell nanocubes and octahedra achieved the comparable free energies of ΔG in the range of -0.17 to -0.36 eV. Therefore, we consider that the kinetic barrier of the rate-determined Tafel step of HER (Figures 4F and S21) for these two surfaces may play an important factor in determining the corresponding facet-dependent catalytic effect for HER (Figures 4A and B).

System	H sites	ΔH (eV)	ΔG (eV)	Fig.
Ru {100}	Ru-Pt	-0.48	-0.25	S22 A
	Ru-Pd	-0.51	-0.28	S22 B
	Ru-Ir	-0.46	-0.22	S22 C
	Ru-Rh	-0.51	-0.28	S22 D
	Ru-Ru	-0.60	-0.36	S22 E
	Ru-top moves to Ru-Ir	-0.46	-0.22	S22 C
	Rh-Ru-Ru (hcp) moves to Ru-Ru	-0.60	-0.36	S22 E
Ru {111}	Pt-Ru-Ru	-0.49	-0.26	S23 A
	Pt-Ru-Rh	-0.40	-0.17	S23 B
	Ru-Pt-Pd	-0.48	-0.25	S23 C
	Ru-Rh-Rh	-0.57	-0.34	S23 D
	Ru-top moves to Pt-Ru-Ru	-0.49	-0.26	S23 A
	Ru-Ru (bridge) moves to Pt-Ru-Ru	-0.49	-0.26	S23 A
Extra {100}	Pt-Pd	-0.42	-0.18	S24 A
	Pt-Ir	-0.49	-0.26	S24 B
	Rh-Pt	-0.49	-0.26	S24 C
	Pd-Rh	-0.51	-0.28	S24 D
	Pt-Pt	-0.51	-0.28	S24 E
Extra {111}	Ir-Pd-Rh	-0.44	0.21	S25

Table S9. Adsorption energy (ΔH) and free energy (ΔG) of H adsorption on Pt {111} and Pt {100} surfaces.

System	H site	ΔH (eV)	ΔG (eV)	Fig.
Pt {111}	bridge	-0.44	-0.21	S26 A
	fcc	-0.55	-0.32	S26 B
	top-Pt	-0.40	-0.16	S26 C
	hcp		Move to bridge	
Pt {100}	bridge	-0.64	-0.40	S26 D
	hcp	-0.76	-0.52	S26 E
	top-Pt	-1.01	-0.78	S26 F

References

1. Park, J. et al. Atomic layer-by-layer deposition of platinum on palladium octahedra for enhanced catalysts toward the oxygen reduction reaction. *ACS Nano* **9**, 2635–2647 (2015).
2. Moulder, J. F., Stickle, W. F., Sobol, P. E. & Bomben, K. D. *Handbook of X-ray Photoelectron Spectroscopy* (Perkin-Elmer, Minnesota, 1992), pp.114–195.
3. Morris, D. et al. Composition-dependent structure and properties of 5- and 15-element high-entropy alloy nanoparticles. *Cell Rep. Phys. Sci.* **2**, 100641 (2021).
4. Hurley, N., McGuire, S. C. & Wong, S. S. Assessing the catalytic behavior of platinum group metal-based ultrathin nanowires using X-ray absorption spectroscopy. *ACS Appl. Mater. Interfaces* **13**, 58253–58260 (2021).
5. Morales, D. M. & Risch, M. Seven steps to reliable cyclic voltammetry measurements for the determination of double layer capacitance. *J. Phys. Energy* **3**, 034013 (2021).
6. Glasscott, M. W. Classifying and benchmarking high-entropy alloys and associated materials for electrocatalysis: a brief review of best practices. *Curr. Opin. Electrochem.* **34**, 100976 (2022).
7. Gilroy, K. D., Ruditskiy, A., Peng, H. C., Qin, D. & Xia, Y. Bimetallic nanocrystals: syntheses, properties, and applications. *Chem. Rev.* **116**, 10414–10472 (2016).
8. Bard, A. J., Faulkner, L. R. & White, H. S. *Electrochemical Methods: Fundamentals and Applications.* (John Wiley & Sons, 2022).